Role of extrusion of the Rand and Sierra de Salinas schists in Late Cretaceous extension and rotation of the southern Sierra Nevada and vicinity

Alan D. Chapman,[1] Steven Kidder,[1] Jason B. Saleeby,[1] and Mihai N. Ducea[2]

Received 24 August 2009; revised 16 March 2010; accepted 4 June 2010; published 15 September 2010.

[1] The Rand and Sierra de Salinas schists of southern California were underplated beneath the southern Sierra Nevada batholith and adjacent Mojave-Salinia region along a shallow segment of the subducting Farallon plate in Late Cretaceous time. Various mechanisms, including return flow, isostatically driven uplift, upper plate normal faulting, erosion, or some combination thereof, have been proposed for the exhumation of the schist. We supplement existing kinematic data with new vorticity and strain analysis to characterize deformation in the Rand and Sierra de Salinas schists. These data indicate that the schist was transported to the SSW from deep to shallow crustal levels along a mylonitic contact (the Rand fault and Salinas shear zone) with upper plate assemblages. Crystallographic preferred orientation patterns in deformed quartzites reveal a decreasing simple shear component with increasing structural depth, suggesting a pure shear dominated westward flow within the subduction channel and localized simple shear along the upper channel boundary. The resulting flow type within the channel is that of general shear extrusion. Integration of these observations with published geochronologic, thermochronometric, thermobarometric, and paleomagnetic studies reveals a temporal relationship between schist unroofing and upper crustal extension and rotation. We present a model whereby trench-directed channelized extrusion of the underplated schist triggered gravitational collapse and clockwise rotation of the upper plate.

Citation: Chapman, A. D., S. Kidder, J. B. Saleeby, and M. N. Ducea (2010), Role of extrusion of the Rand and Sierra de Salinas schists in Late Cretaceous extension and rotation of the southern Sierra Nevada and vicinity, *Tectonics*, *29*, TC5006, doi:10.1029/2009TC002597.

1. Introduction

[2] The Rand and Sierra de Salinas schists (referred to here as "the schist") and related Pelona and Orocopia schists have long attracted interest due their underthrust position relative to older Mesozoic batholith over much of southern California [*Ehlig*, 1958; 1981; *Graham and England*, 1976; *Haxel and Dillon*, 1978; *Jacobson*, 1983, 1995; *Jacobson et al.*, 1988, 2007]. Most workers agree that the deposition and emplacement of the schist occurred during an episode of shallow subduction related to the Laramide orogeny [*Jacobson et al.*, 2007, and references therein]. Comparatively less is understood, however, regarding mechanisms underlying schist exhumation. Geochronologic, thermochronometric, and thermobarometric studies indicate a temporal link between schist unroofing and major upper crustal extension [*Pickett and Saleeby*, 1993; *Jacobson*, 1995; *Kistler and Champion*, 2001; *Barth et al.*, 2003; *Grove et al.*, 2003; *Kidder et al.*, 2003; *Kidder and Ducea*, 2006; *Saleeby et al.*, 2007]. As discussed below, schist ascent coincided with clockwise rotation of the southern Sierra Nevada batholith (SNB) [*Kanter and McWilliams*, 1982; *McWilliams and Li*, 1985; *Plescia et al.*, 1994].

[3] Existing models for the exhumation of the northern (i.e., Rand and Sierra de Salinas) and southern (i.e., Pelona and Orocopia) schists invoke return flow [*Oyarzabal et al.*, 1997; *Jacobson et al.*, 2002; *Saleeby*, 2003; *Saleeby et al.*, 2007], isostatically driven uplift [*Jacobson et al.*, 2007], upper plate normal faulting [e.g., *Jacobson et al.*, 1996], erosion [*Yin*, 2002], or some combination thereof. We discuss these models in light of new field and microstructural work and conclude that an alternative exhumation mechanism, channelized extrusion, played an important role in exhumation.

[4] Here we address unresolved issues related to schist emplacement including (1) the mechanisms of schist underthrusting and exhumation and (2) the relationship between schist emplacement and upper plate extension and rotation in the southern Sierra Nevada and adjacent areas. We compile new and published structural data from the principal exposures of the schist indicating noncoaxial lower plate transport to the SSW at high structural levels and increasing coaxial component of deformation with structural depth. We propose that Late Cretaceous trench-directed channelized extrusion in the underplated schist led to high magnitude extension, deep exhumation, and westward deflection of the upper plate batholith above the flowing channel.

2. Geologic Background

2.1. Rand and Sierra de Salinas Schists

[5] The Rand and Sierra de Salinas schists are the northernmost exposures of a high P–intermediate to high T

[1] Division of Geological and Planetary Sciences, California Institute of Technology, Pasadena, California, USA.

[2] Department of Geosciences, University of Arizona, Tucson, Arizona, USA.

0278-7407/10/2009TC002597

terrane that underlies much of southern California and southwestern Arizona along detachment structures [*Cheadle et al.*, 1986; *Li et al.*, 1992; *Malin et al.*, 1995; *Yan et al.*, 2005]. Intensive study of the schist indicates that it formed by deposition of Late Cretaceous arc-derived detritus at the North America–Farallon plate margin and was underplated and metamorphosed along a shallow segment of the subducting Farallon slab [*Grove et al.*, 2003; *Saleeby*, 2003]. The spatial distribution of the schist (Figure 1) was controlled by the geometrical evolution of the Farallon slab. As the slab was underthrust to the east beneath North America in the Late Cretaceous, a south to north inflection from shallow to moderate subduction trajectories developed, resembling a regional lateral ramp in the subduction megathrust. This left the lithospheric mantle of the greater SNB intact, while first removing the mantle and subsequently underplating schist directly beneath the southern SNB and the adjacent Salinia terrane [*Malin et al.*, 1995; *Ducea and Saleeby*, 1998; *Saleeby*, 2003; *Nadin and Saleeby*, 2008]. Intense contractile deformation along the shallow megathrust flat removed virtually the entire fore-arc and frontal arc plutonic zone by subduction erosion, leading to rapid uplift and denudation of the residual arc to midcrustal levels [*Saleeby*, 2003; *Saleeby et al.*, 2007; *Ducea et al.*, 2009]. During the unroofing of the Cretaceous arc, the transport direction in the subduction wedge reversed, and the schist was educted from the subduction zone [*Saleeby et al.*, 2007, Figure 7; *Ducea et al.*, 2009, Figure 3].

2.2. Kern Canyon-Proto-White Wolf Fault System

[6] Here we review temporal and kinematic relations between the principal members of the integrated Kern Canyon–White Wolf system [after *Nadin and Saleeby*, 2008], as they are important for both the contractile and extensional phases of regional deformation related to schist underplating. Continuity between the Kern Canyon fault and the White Wolf fault was first emphasized by *Ross* [1986], although subsequent workers have not realized the significance of this relationship. Dextral slip along the Kern Canyon–White Wolf fault zone (abbreviated as KWF below) increases southward from zero at ~36.7° N to ~40 km near the Tejon embayment. The dip slip component also increases southward to as much as ~15 km near the Tejon embayment. Dextral displacement along the Kern Canyon segment is constrained to ~88–80 Ma, and bracketed to between 98 and 70 Ma along the White Wolf segment. The KWF acted as a transfer structure between a highly extended and exhumed southeastern block and a significantly less extended and exhumed northwestern block. Northwest striking extensional fracture swarms are common southeast of, and rare northwest of, the KWF (Figure 1).

[7] Following early Cenozoic quiescence the KWF was reactivated as a transfer structure for lower magnitude extension in the early Neogene. In the Quaternary the Kern Canyon segment was again remobilized as a west side up normal fault, while eastern and western segments of the White Wolf fault functioned as a sinistral fault and a north directed thrust, respectively [*Mahéo et al.*, 2009; *Saleeby et al.*, 2009; *Nadin and Saleeby*, 2010].

2.3. Constraints on Rotation and Tilting

[8] The Sierra Nevada block is a predominantly NNW trending composite batholith with juvenile batholithic crust extending to ≥ 35 km depth [*Ruppert et al.*, 1998; *Saleeby et al.*, 2003; 2007]. South of 35.5°N latitude, the depth of exposure increases markedly while structural and petrologic patterns in the batholith abruptly swing up to 90° westward, taking on an east-west trend [*Kanter and McWilliams*, 1982; *McWilliams and Li*, 1983; *Wood and Saleeby*, 1997; *Nadin and Saleeby*, 2008] (Figure 1 insets). This trend continues from the southernmost SNB into the northwestern Mojave Desert and adjacent Salinian block when restored along the San Andreas fault. A poorly preserved zone of sinistral transcurrent faulting between the San Gabriel Mountains and the Peninsular Ranges [*May*, 1989] (Figure 1 top left inset) probably represents a "mirror image" of clockwise rotation in the southern SNB. There is no evidence for rotation north of the KWF. Despite concerted efforts to constrain vertical axis rotation in the southern SNB [e.g., *Kanter and McWilliams*, 1982; *McWilliams and Li*, 1985; *Plescia et al.*, 1994], the timing of and mechanisms behind the deflection remain poorly understood. Existing explanations for the change in trend include: (1) post-Cretaceous oroclinal bending related to dextral transpression along the North America–Farallon plate margin [*Burchfiel and Davis*, 1981; *McWilliams and Li*, 1985]; (2) early Miocene transtension in the Mojave Desert [*Ross et al.*, 1989; *Dokka and Ross*, 1995]; (3) Late Cretaceous west directed intra-arc thrusting [*May*, 1989]; and (4) Late Cretaceous coupling between westward displaced underplated Rand and Sierra de Salinas schists and associated upper plate batholithic assemblages [*Malin et al.*, 1995; *Saleeby*, 2003].

[9] In contrast to the rotational history of the southernmost SNB and Salinia, the timing and magnitude of regional northward tilting in the area are well understood (Figure 2). Integrated thermochronometric and thermobarometric data from the southwestern SNB track the cooling, ~25° northward tilting, and unroofing of deep batholithic rocks from ~9 kbar conditions at circa 98 Ma to midcrustal levels (~4 kbar) by circa 95 Ma [*Malin et al.*, 1995; *Saleeby et al.*, 2007] (Figure 2a). This uplift of the upper plate immediately preceded underplating and cooling of the Rand Schist. The cooling path of the Rand schist of the San Emigdio Mountains merges with that of the upper plate beginning at circa 86 Ma [*Grove et al.*, 2003]. In Salinia, upper plate rocks ascended from ~7.5 kbar to the upper crust between circa 81 and 71 Ma, tilting the region ~30° to the northeast [*Kidder et al.*, 2003] (Figure 2b). In the Sierra de Salinas, juxtaposition of lower plate schist with the upper plate also took place in the Late Cretaceous [*Barth et al.*, 2003; *Kidder and Ducea*, 2006]. Thermochronologic data from the lower plate schist of the Rand Mountains and adjacent Late Cretaceous plutons in the Fremont Peak region and migmatites in the Buttes indicate a similar relationship between cooling in the upper and lower plates [*Fletcher et al.*, 2002;

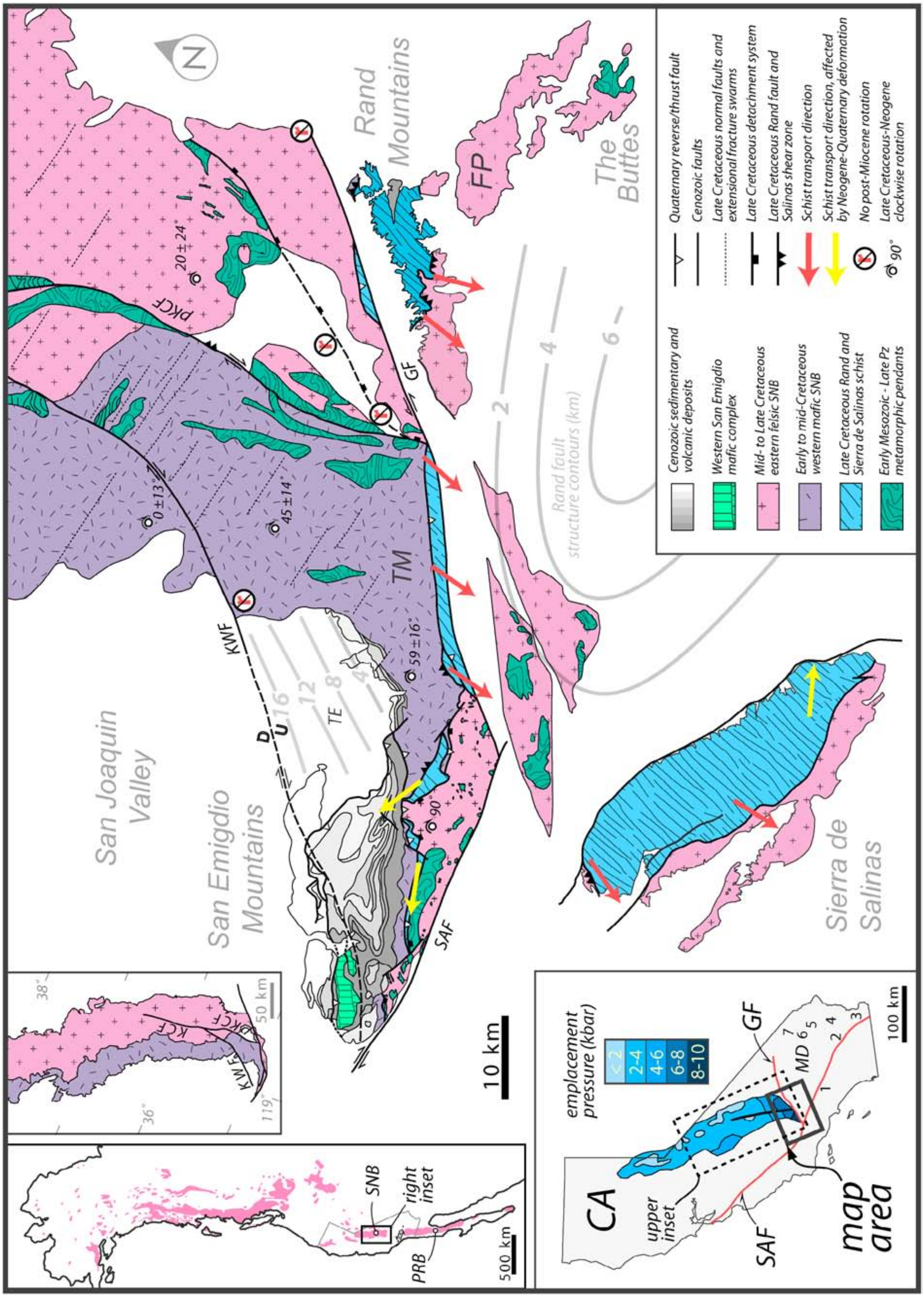

Rand Mountains
The Buttes
FP
San Joaquin Valley
San Emigdio Mountains
Sierra de Salinas
TM
TE
KWF
pKCF
GF
SAF
Rand fault structure contours (km)
10 km
Cenozoic sedimentary and volcanic deposits
Western San Emigdio mafic complex
Mid- to Late Cretaceous eastern felsic SNB
Early to mid-Cretaceous western mafic SNB
Late Cretaceous Rand and Sierra de Salinas schist
Early Mesozoic - Late Pz metamorphic pendants
Quaternary reverse/thrust fault
Cenozoic faults
Late Cretaceous normal faults and extensional fracture swarms
Late Cretaceous detachment system
Late Cretaceous Rand fault and Salinas shear zone
Schist transport direction
Schist transport direction, affected by Neogene-Quaternary deformation
No post-Miocene rotation
Late Cretaceous-Neogene clockwise rotation
emplacement pressure (kbar)
<2
2-4
4-6
6-8
8-10
CA
upper inset
map area
MD
100 km
SNB
right inset
PRB
500 km
50 km

Figure 1

Grove et al., 2003] ("Central Mojave metamorphic core complex," Figure 2c). One notable feature apparent in Figure 2 is that the Salinian block and Rand Mountains vicinity cooled ~20 Myr later than the Tehachapi and San Emigdio Mountains.

2.4. Rand Fault and Salinas Shear Zone

[10] In the Rand, Tehachapi, and San Emigdio Mountains, the Rand schist crops out beneath deeply exhumed mafic to intermediate composition SNB assemblages (the "upper plate") along the remains of the Late Cretaceous subduction megathrust flat (the Rand fault) immediately south of the lateral ramp. In Salinia, a correlative structure (the Salinas shear zone) separates middle crustal Cretaceous hornblende-quartz diorites from the underlying Sierra de Salinas schist [*Kidder and Ducea*, 2006; *Ducea et al.*, 2007]. The presence of an inverted metamorphic field gradient, i.e., an upward increase in temperature, is a characteristic feature of northern and southern schists [e.g., *Ehlig*, 1958; *Sharry*, 1981; *Graham and Powell*, 1984; *Jacobson*, 1995; *Kidder and Ducea*, 2006]. In both the southern SNB and Salinia, a narrow (<10 m) zone of mylonite and cataclasite marks the contact between the schist and upper plate. Shear sense determinations were made within the schist, at the base of the upper plate, and in intervening mylonites to evaluate the direction of schist transport with respect to the upper plate. The following sections describe the geology and upper plate–lower plate contact relations in the Rand, Tehachapi, Sierra de Salinas, and San Emigdio localities.

3. Results

3.1. Rand Mountains

[11] The Rand fault ("fault I" of *Nourse* [1989], and the "Rand thrust" of *Postlethwaite and Jacobson* [1987]) is exposed along the northern and southern margins of the type Rand schist, separating it from upper plate amphibolite grade gneisses in the northeast and the Atolia Quartz Monzonite in the southwest (Figure 3). The southern contact between the schist and Atolia Quartz Monzonite is marked by a narrow (<10 m) zone of mylonite to cataclasite. Mylonitic stretching lineations are generally subhorizontal and oriented oblique to perpendicular to the trace of the Rand fault. *Postlethwaite and Jacobson* [1987] and *Nourse* [1989] discern at least two different episodes of shearing in structurally complex noncoaxial fabrics proximal to the Rand fault. Evidence for an early, upper plate to the southwest tectonic event is locally preserved along the shear zone and variably overprinted by top to the northeast structures. Retrograde metamorphic reactions proceeded in concert with mylonitization, suggesting progressive shearing during decreasing temperature.

3.2. Sierra de Salinas

[12] The schist of Sierra de Salinas comprises the largest exposure of the schist. It has been translated ~330 km from a location ~75 km south of the San Emigdio mountains along the San Andreas fault [*Powell*, 1993] and tilted such that it exposes a ~2.5 km thick structural section of predominantly metasandstone.

[13] Measurements of the strike and dip of foliation and rake of mineral stretching lineations in the schist and upper plate are shown in Figure 4. Lineations in the schist dominantly trend northeast–southwest, but show some scatter. The schist is notably less lineated at deeper levels in terms of the abundance of lineated outcrops (Figure 4a) and, where present, the strength of lineations. The decrease in lineation abundance may not simply be attributed to a decrease in strain with depth, as highly transposed quartz veins are observed at all structural levels, and may instead signify a change in the shape of the finite strain ellipsoid with depth. Differences in foliation between the central and northern area are interpreted as a late rotation roughly about the lineation direction. A single shear sense determination made in the southern area is considered dubious due to recent faulting.

[14] Outcrop scale shear sense indicators are rare in the Sierra de Salinas, but were found in thin sections of both the schist and upper plate. The most common shear sense indicators are biotite fish, although feldspar, sphene, clinopyroxene, hornblende, and muscovite fish are also present. Mineral fish are considered here to be any isolated grains of reduced size showing morphologic similarity to the fish described by *Lister and Snoke* [1984], *Pennacchioni et al.* [2001] or *ten Grotenhuis et al.* [2003]. In most cases, fish are included in or between fairly equant or amoeboid quartz grains in foliation-parallel quartz bands (e.g., Figures 5a

Figure 1. Tectonic map of southern Sierra Nevada basement with related elements of northern Mojave and Sierra de Salinas restored along San Andreas and Garlock faults. For compactness, Sierra de Salinas is shown ~50 km north of its pre-Neogene location. Distribution of Mesozoic and early Tertiary arc plutons in the North American Cordillera (top left inset) after *Miller et al.* [2000]. Primary zonation and structures of the Sierra Nevada batholith (upper right inset) from *Nadin and Saleeby* [2008] and *Saleeby et al.* [2007]. Detachment systems from *Wood and Saleeby* [1997]. Transport directions of Rand schist from *Nourse* [1989], *Wood and Saleeby* [1997], and this study. Paleomagnetic data from *Kanter and McWilliams* [1982], *McWilliams and Li* [1983], and *Wilson and Prothero* [1997]. Pluton emplacement pressures in California index map (bottom inset) from *Ague and Brimhall* [1988], *Pickett and Saleeby* [1993], and *Nadin and Saleeby* [2008]. Numbers 1–7 in bottom inset refer to locations: 1, San Gabriel Mountains; 2, Orocopia Mountains; 3, Gavilan Hills; 4, Iron Mountains; 5, Old Woman Mountains; 6, Granite Mountains; 7, New York Mountains. Abbreviations FP, Fremont Peak; GF, Garlock fault; KCF, Kern Canyon fault; KWF, Kern Canyon/proto-White Wolf fault (dashed where concealed); pKCF, proto-Kern Canyon fault; MD, Mojave Desert; PRB, Peninsular Ranges batholith; SAF, San Andreas fault; SNB, Sierra Nevada batholith; TE, Tejon embayment; TM, Tehachapi Mountains.

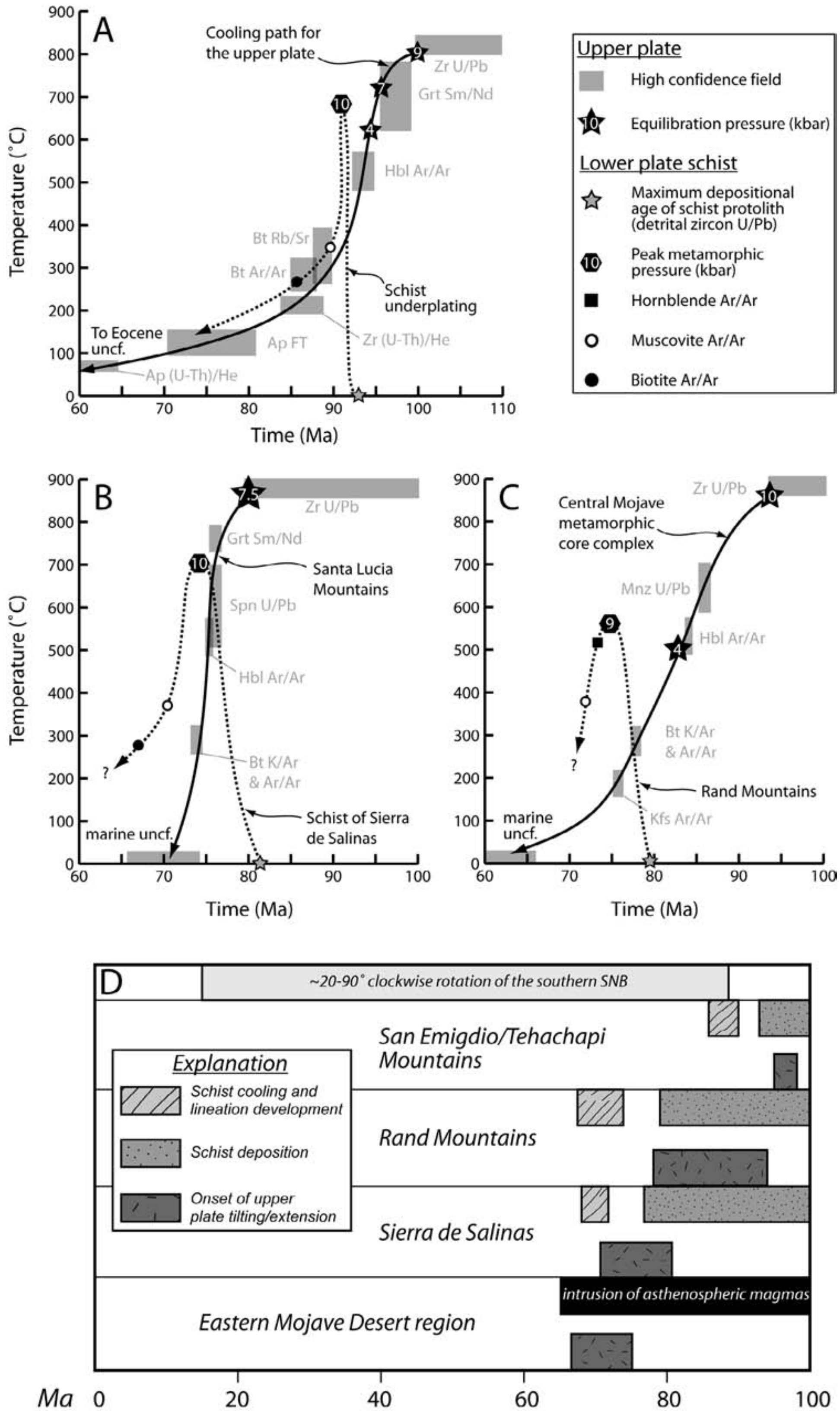
A
Cooling path for the upper plate
Zr U/Pb
Grt Sm/Nd
Hbl Ar/Ar
Bt Rb/Sr
Bt Ar/Ar
Schist underplating
To Eocene uncf.
Ap FT
Zr (U-Th)/He
Ap (U-Th)/He
Temperature (°C)
Time (Ma)
Upper plate
High confidence field
Equilibration pressure (kbar)
Lower plate schist
Maximum depositional age of schist protolith (detrital zircon U/Pb)
Peak metamorphic pressure (kbar)
Hornblende Ar/Ar
Muscovite Ar/Ar
Biotite Ar/Ar
B
Zr U/Pb
Grt Sm/Nd
Santa Lucia Mountains
Spn U/Pb
Hbl Ar/Ar
Bt K/Ar & Ar/Ar
Schist of Sierra de Salinas
marine uncf.
C
Central Mojave metamorphic core complex
Mnz U/Pb
Hbl Ar/Ar
Bt K/Ar & Ar/Ar
Rand Mountains
Kfs Ar/Ar
marine uncf.
D
~20-90° clockwise rotation of the southern SNB
San Emigdio/Tehachapi Mountains
Explanation
Schist cooling and lineation development
Schist deposition
Onset of upper plate tilting/extension
Rand Mountains
Sierra de Salinas
intrusion of asthenospheric magmas
Eastern Mojave Desert region
Ma

Figure 2

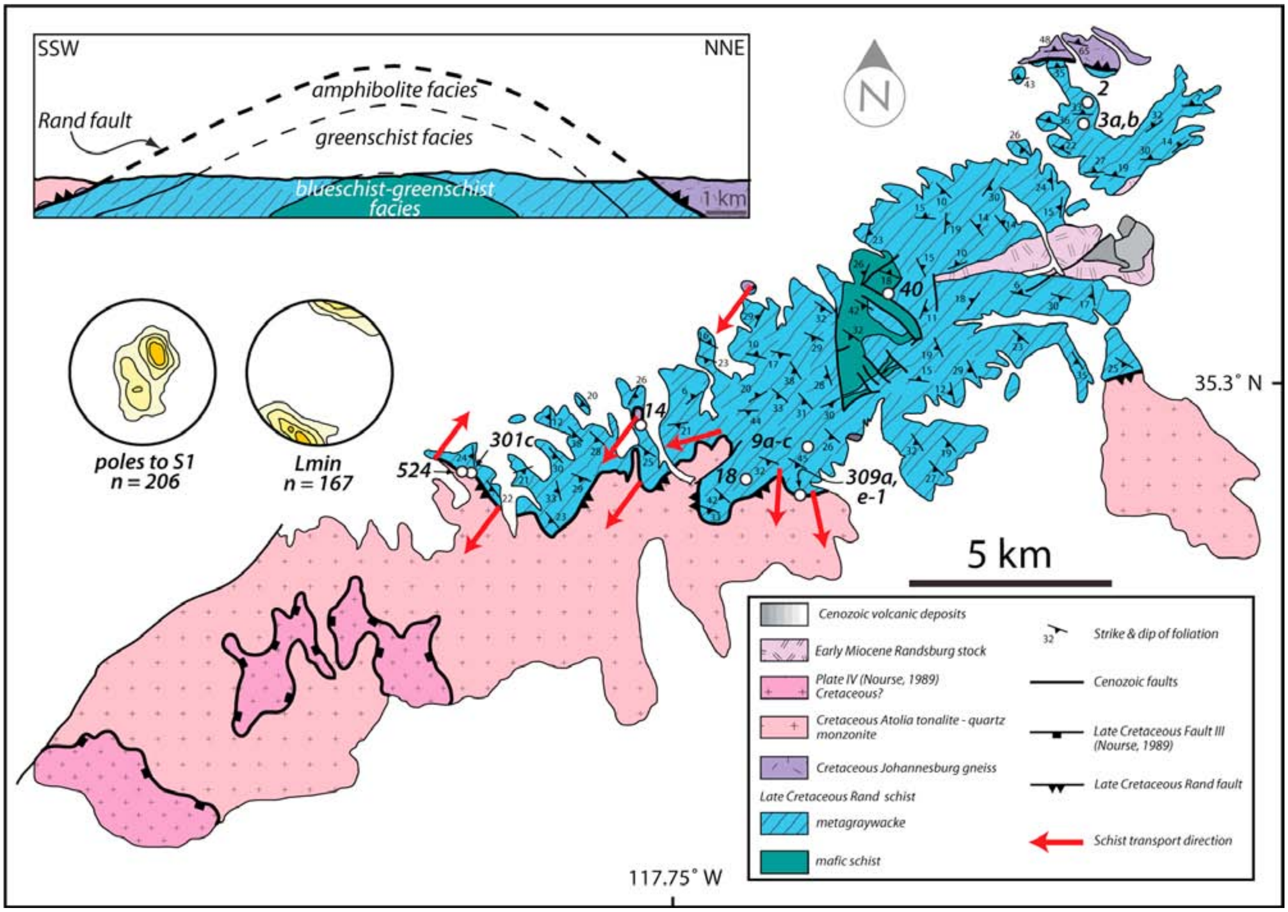

Figure 3. Simplified geologic map of the Rand Mountains. Geology after *Dibblee* [1967], *Vargo* [1972], *Postlethwaite and Jacobson* [1987], and *Nourse* [1989]. Generalized NNE to SSW cross section after *Postlethwaite and Jacobson* [1987]. Rand schist structural data are equal-area lower hemisphere stereographic projections of the orientation of mineral lineations (Lmin) (contour interval 4σ) and poles to mylonitic foliation (S1) (contour interval 3σ) [*Postlethwaite and Jacobson*, 1987]. Circles show locations of quartz CPO measurements.

Figure 2. Time-temperature paths for upper plate rocks (solid pattern) and the Sierra de Salinas and Rand schist (dashed pattern) in (a) the Tehachapi and San Emigdio Mountains, (b) the Salinian block, and (c) the central Mojave metamorphic core complex and Rand Mountains. Note that the time-temperature data for the central Mojave metamorphic core complex (upper plate) and the Rand Mountains (lower plate schist) represent a highly oblique section from the upper to the lower plate. Lower plate thermochronologic constraints from *Jacobson* [1990], *Barth et al.* [2003], and *Grove et al.* [2003]. Upper plate thermochronologic constraints from *Mattinson* [1978], *Kistler and Champion* [2001], *Ducea et al.* [2003], and *Kidder et al.* [2003] (Salinian block); *Henry and Dokka* [1992], *Fletcher et al.* [2002], and P. Gans (written communication, 2010) (central Mojave Desert); and *Saleeby et al.* [1987], *Naeser et al.* [1990], *Pickett and Saleeby* [1994], and *Saleeby et al.* [2007] (Tehachapi and San Emigdio Mountains). Thermobarometric constraints from: *Kidder et al.* [2003] and *Kidder and Ducea* [2006] (Salinian block); *Henry and Dokka* [1992] and *Jacobson* [1995] (central Mojave Desert); and *Pickett and Saleeby* [1993] (Tehachapi and San Emigdio Mountains). Mineral abbreviations Ap, apatite; Bt, biotite; Kfs, K-feldspar; Grt, garnet; Hbl, hornblende; Mnz, monazite; Ms, muscovite; Spn, sphene; Zr, zircon. Other abbreviations: FT, fission track; uncf., unconformity. (d) Summary of kinematic events for the southern SNB, Salinia, and eastern Mojave Desert region. Timing of rotation from *Kanter and McWilliams* [1982], *McWilliams and Li* [1983], and *Saleeby et al.* [2007]. Schist deposition and cooling age data from *Grove et al.* [2003] and *Barth et al.* [2003]. Upper plate tilting/extension from *Fletcher et al.* [2002], *Kidder et al.* [2003], *Saleeby et al.* [2007], and *Wells and Hoisch* [2008]. Intrusion age of asthenospheric magmas from *Leventhal et al.* [1995].

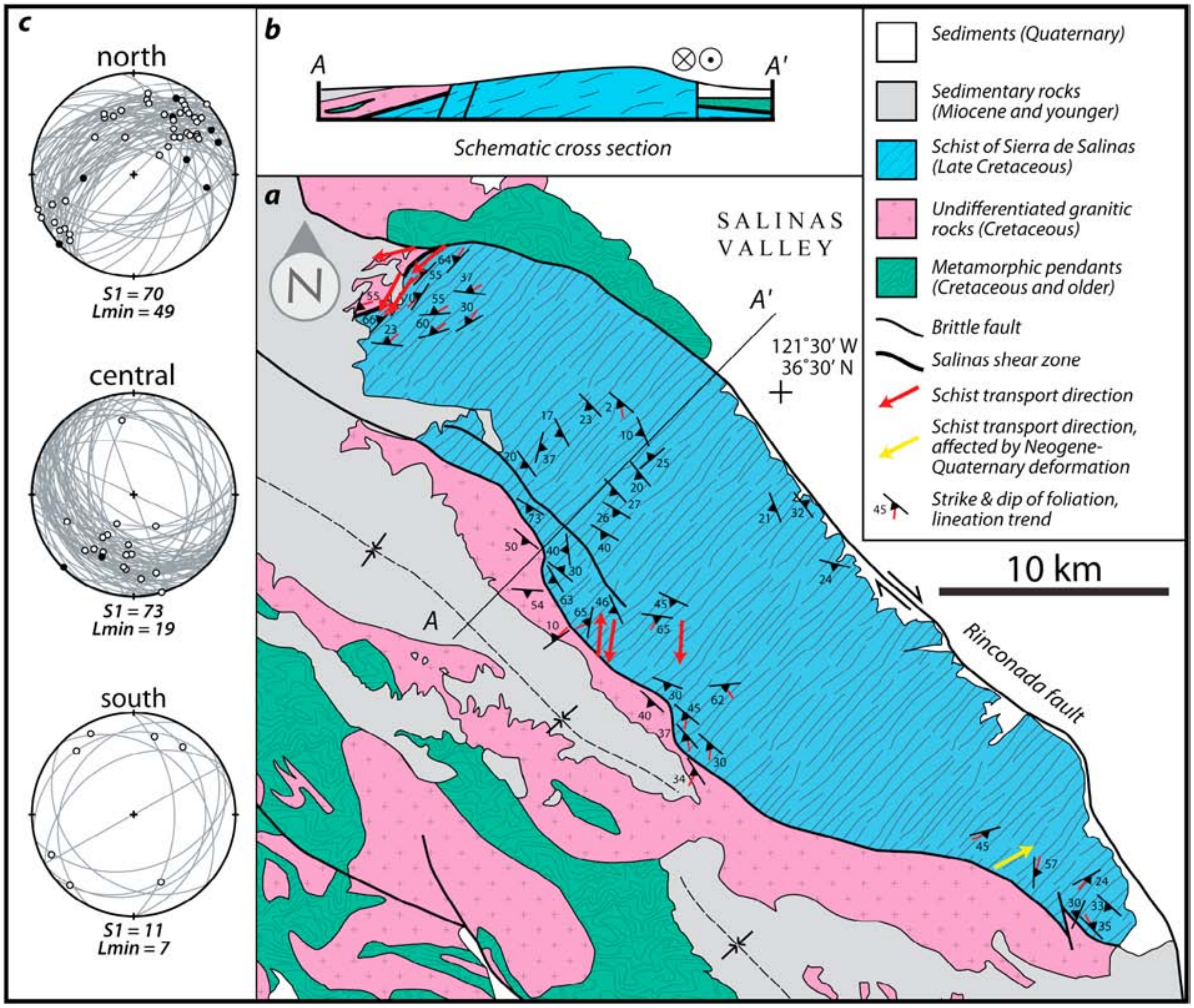

Figure 4. (a) Geologic map of the Sierra de Salinas based on *Ross* [1976], *Dibblee* [1974], *Kidder and Ducea* [2006] and this study. All plotted attitudes were made by the authors. (b) Schematic cross section across the Sierra de Salinas. (c) Equal-area lower hemisphere stereonets from northern, central and southern portions of the map area showing foliation (S1) and lineation (Lmin) measurements. Upper plate lineation shown as solid dots, schist lineations as open dots.

and 5b). Mineral fish develop during mylonitic deformation [*Lister and Snoke*, 1984], thus substantial annealing grain growth or high temperature grain boundary migration recrystallization occurred in quartz in nearly all observed samples following an early phase of mylonitization. Only fish inclined in the same direction to both the overall foliation and local boundaries of quartz bands were used as shear sense indicators (e.g., Figure 5b). Near the schist–upper plate contact, highly deformed fine-grained asymmetric quartz (Figure 5c) and C′ shear bands [*Passchier and Trouw*, 2005] associated with retrograde chlorite (Figure 5d) are also observed. Shear sense indicators were tallied without knowledge of sample orientation during petrographic analysis to avoid bias. Ten of 44 samples contain a sufficiently large population and uneven distribution of top to the northeast (TTN) and top to the southwest (TTS) shear sense indicators such that there is high probability of noncoaxial flow (Figure 6). "High probability" indicates a greater than 95% likelihood that a given distribution was not sampled from an evenly distributed population.

[15] Shear sense in greenschist facies (i.e., late) mylonites near the schist–upper plate contact are unambiguously TTN (Figures 5 and 6). Late shear sense indicators are far less abundant than amphibolite facies (i.e., early) fabrics at deep structural levels in the schist. Away from the shear zone in the schist, TTS shear indicators are slightly more abundant than TTN features (130 versus 116). Two samples of the schist show a TTS shear sense and two are TTN.

3.3. San Emigdio Mountains

[16] Uplift of basement and sedimentary cover strata in the San Emigdio Mountains is controlled by Pliocene-Quaternary north-south compression between the big bend

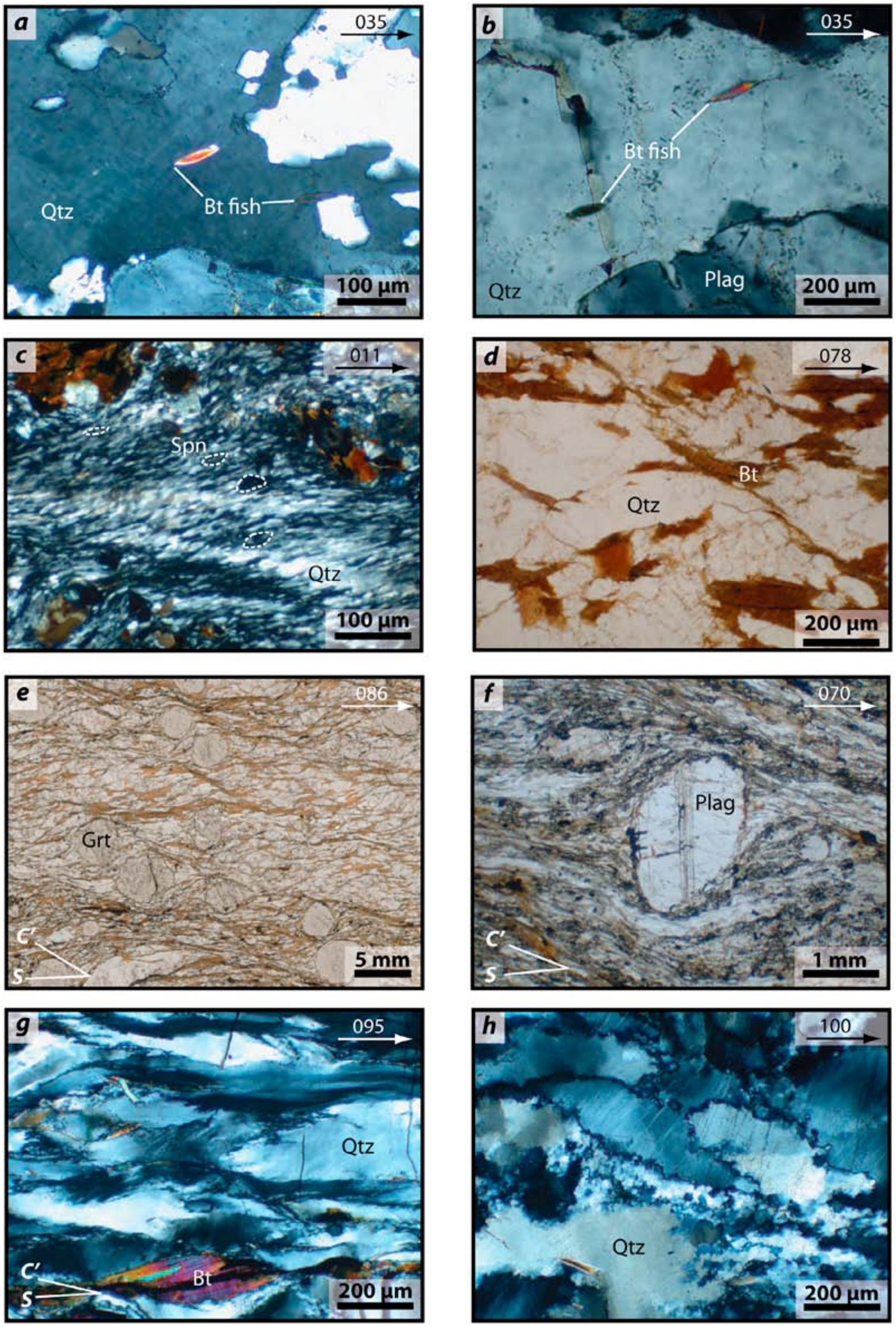
a
035
Qtz
Bt fish
100 µm
b
035
Bt fish
Qtz
Plag
200 µm
c
011
Spn
Qtz
100 µm
d
078
Bt
Qtz
200 µm
e
086
Grt
C′
S
5 mm
f
070
Plag
C′
S
1 mm
g
095
Qtz
C′
S
Bt
200 µm
h
100
Qtz
200 µm

Figure 5

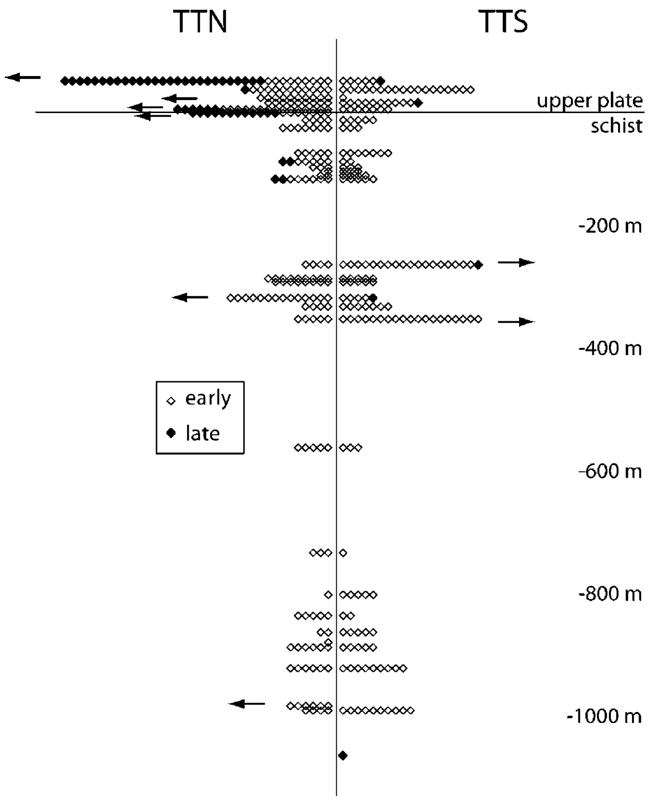

Figure 6. Graphical representation of shear sense indicators. Top to the northeast (TTN) and top to the southwest (TTS) indicators are tallied versus structural depth. Each point (n = 402) represents a single indicator. Solid symbols represent indicators associated with retrograde metamorphism or overprinting relationships, mainly C′ shear bands or asymmetric quartz (49 TTN, 5 TTS). Open symbols represent shear sense indicators associated with early deformation. Arrows indicate the position of individual samples showing a consistent sense of shear and the associated direction of upper plate motion.

in the San Andreas fault and the Pleito fault zone [*Davis*, 1983; *Dibblee*, 1986] (Figures 1 and 7). Cretaceous plutonic and associated framework metamorphic rocks comprise the bulk of the basement complex in the San Emigdio Mountains [*Ross*, 1989]. This basement complex is subdivided into four principal assemblages. First is a collection of shallow level (3–4 kbar) eastern SNB affinity granitoids and metamorphic pendant rocks referred to as the Pastoria plate (modified after *Crowell* [1952]). The Pastoria fault, a member of the Late Cretaceous–Paleocene southern Sierra detachment system of *Wood and Saleeby* [1997] reactivated in Pliocene-Quaternary time as a south dipping thrust, lies at the base of the Pastoria plate. Beneath the Pastoria fault lies the western continuation of Early to mid-Cretaceous deep-level SNB rocks defined in the Tehachapi Mountains as the Tehachapi complex [*Saleeby et al.*, 2007]. Continuity of the Tehachapi complex into the San Emigdio Range leads us to rename the entire deep batholithic complex as the Tehachapi–San Emigdio complex. A third basement assemblage consisting of shallow level (<3 kbar) western Sierra Nevada Foothills belt rocks [*James et al.*, 1993; *Reitz*, 1986] crops out in the westernmost San Emigdio Mountains, and is named here the western San Emigdio mafic complex.

[17] The Tehachapi–San Emigdio complex sits tectonically above the Rand schist along the polyphase Rand fault. The Rand schist is juxtaposed against the Tehachapi–San Emigdio complex along the remains of a locally ductile to brittle low-angle detachment fault system that likely correlates with the type Rand fault [*Postlethwaite and Jacobson*, 1987; *Nourse*, 1989]. This fault is largely remobilized as a south dipping thrust fault with the Rand schist in the hanging wall and the Tehachapi–San Emigdio complex in the footwall.

[18] The Pastoria plate overlies the contact between the Tehachapi–San Emigdio complex and the Rand schist in two locations in the San Emigdio Mountains, partitioning the schist into western, central, and eastern domains. In each domain, both the schist and the Tehachapi–San Emigdio complex contain gently plunging, E–W trending stretching lineations and fold hinges that are most penetrative within ~100 m of the Rand fault. Compositional layering in the schist is generally parallel to that of the Tehachapi–San Emigdio complex and dips ~45° to the south.

[19] In each domain, lineations are recorded first in amphibolite facies assemblages, and are overprinted by parallel greenschist facies fabrics and subsequent brittle deformation. We interpret these overprinting relationships to represent progressive shearing during exhumation of the schist and upper plate through the ductile-brittle transition. In 19 of 25 locations where shear sense determinations were possible (Table 1), microstructures are indicative of schist transport to the west (top to the east) (Figure 7). Evidence for west directed transport of the schist is best expressed in

Figure 5. Photographs of microstructural features in the Sierra de Salinas (Figures 5a–5d) and the Rand schist of the San Emigdio Mountains (Figures 5e–5h). Photographs are upright and lineation azimuth is inscribed in each. (a) Typical biotite fish in a quartz band in the schist; xpl. (b) Two biotite fish in a quartz band and a plagioclase grain showing undulose extinction in the schist; xpl. (c) Quartz ribbons in a late upper plate mylonite showing sphene fish (outlined) and inclined recrystallized quartz grains (TTN); xpl. (d) Shear band from top left to lower right in the schist. Quartz and partially chloritized biotite grains are deflected into the shear band (TTN); ppl. (e) Top to the east (TTE) S-C fabrics and garnet porphyroblasts surrounded by asymmetric pressure shadows of quartz; ppl. (f) Plagioclase sigma porphyroclast and S-C fabrics (TTE); ppl. (g) Sample 06SE66. Elongate quartz grains with sweeping undulatory extinction and recrystallization by subgrain rotation. Note S-C fabrics and biotite fish (TTE); xpl. (h) Sample 08SE473. Quartz with sutured grain boundaries and recrystallization by subgrain rotation and grain boundary migration; xpl. Mineral abbreviations Bt, biotite; Grt, garnet; Plag, plagioclase; Qtz, quartz; Spn, sphene. Other abbreviations: ppl, plane-polarized light; xpl, cross-polarized light.

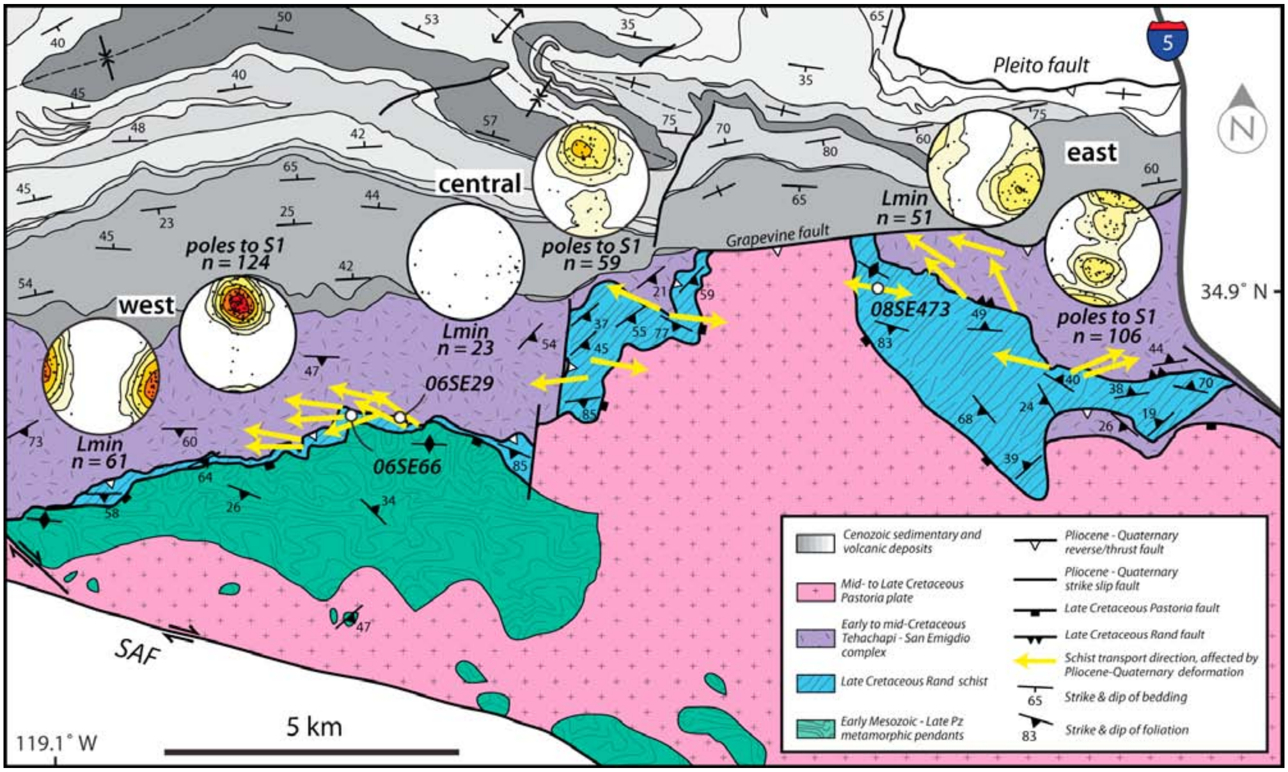

Figure 7. Simplified geologic map of the San Emigdio Mountains. Geology from *Ross* [1989], *Dibblee* [1973], and this study. Equal-area lower hemisphere stereographic projections (Kamb contours at 2σ, 4σ, 6σ, 10σ, 14σ, and 20σ) of the orientation of mineral lineations (Lmin) and poles to mylonitic foliation (S1) are shown along western, central, and eastern domains of the Rand fault. Circles show locations of EBSD measurements. Abbreviations as in Figure 1.

type II S-C mylonites [*Lister and Snoke*, 1984], asymmetric garnet and plagioclase porphyroclasts, and mica fish (e.g., Figures 5e, 5f, and 5g). The extensional fabric is fairly homogeneous within the lower ~500 m of the upper plate, the upper ~10 m of the Rand schist, and intervening Rand fault mylonites; however, with increased structural depth in the schist (>10 m from the Rand fault), lineations are less penetrative, shear sense indicators commonly conflict at the outcrop scale, quartz veins are more symmetrically transposed parallel to the foliation, and boudinaged quartz + plagioclase layers within less competent metasandstone are more symmetric, indicating dominantly coaxial flattening within the schist > 10 m from the Rand fault. Both coaxial and noncoaxial fabrics are associated with retrograde paragenesis, indicating roughly coeval development of fabrics near the contact (noncoaxial) and > 10 m from the contact (coaxial).

3.4. Tehachapi Mountains

[20] Tehachapi Range basement rocks south of the Garlock fault consist of relatively shallow-level (<3.5 kbar) eastern SNB assemblages that resemble the Pastoria plate. North of the Garlock fault, basement rocks of the Tehachapi Mountains consist primarily of deep-level (8–11 kbar) SNB tonalites, diorites and gabbros that extend to the north in overall structural continuity with shallower level rocks of the southern SNB autochthon [*Pickett and Saleeby*, 1993; *Saleeby et al.*, 2003, 2007]. The deep-level SNB rocks of this region constitute a relatively thin tectonic layer above the Rand schist, thickening to the north above the lateral ramp in the Rand fault [*Malin et al.*, 1995; *Yan et al.*, 2005] (Figure 8). The Rand schist of this area crops out primarily as an ENE–WSW striking fault-bounded sliver that has emerged through overlying plates to exposure levels by oblique sinistral motion along the main branch of the Garlock fault and north directed reverse motion along the north branch of the Garlock fault. A small half window through the Rand fault is preserved near the western end of the Garlock fault. The basal domain of the Tehachapi–San Emigdio complex in the Tehachapi range is comprised mainly of the White Oak diorite gneiss, a tectonic mixture of amphibolite to locally retrograde greenschist facies dioritic and subordinate tonalitic, gabbroic, and mylonitic gneisses and cataclasites.

[21] Structural and thermochronometric data suggest that the White Oak diorite gneiss constitutes the structural base of the Tehachapi–San Emigdio complex throughout much of the Tehachapi range [*Saleeby et al.*, 2007]. The dominant structural fabric of the White Oak unit is that of strong attenuation along moderately north dipping anastomosing ductile to brittle shear bands (Figure 9). In most locations

Table 1. Sample Information and Shear Sense Determinations From the San Emigdio Mountains

Field Location	Lithology	UTM Easting[a]	UTM Northing[a]	Distance to Rand Fault[b] (m)	Shear Sense	Schist Transport Azimuth	Criteria[c]
08SE194	Rand fault mylonite	231760	3864257	667	top E	286	AP
08SE156	Rand fault mylonite	321144	3864254	530	top E	302	AP
08SE198	sheared upper plate paragneiss	321810	3863870	376	top SE	334	AP
08SE172	Rand fault mylonite	321547	3863586	88	top E	314	AP
06SE24	Rand fault ultramylonite	310535	3862054	65	top E	287	SC
06SE25	sheared upper plate diorite	310551	3862034	46	top E	288	AP
06SE77	Rand fault mylonite	311141	3861938	40	top E	284	AP, SC
06SE16	sheared upper plate paragneiss	310569	3861996	17	top E	266	AP, SC
06SE63	Rand fault mylonite	310684	3861986	8	top E	266	SC
06SE31	Rand fault mylonite	311250	3861882	0	top E	250	AP, SC
07SE112	Rand fault mylonite	315081	3863988	0	top E	294	AP, SC
07SE114	Rand fault mylonite	315144	3863864	0	top E	283	SC
07SE135	sheared upper plate paragneiss	315748	3863559	0	top W	97	AP, SC
08SE270	sheared upper plate diorite	309137	3861143	0	top E	275	AP
08SE303	Rand fault mylonite	309822	3861321	0	top E	280	SC, AP
08SE347	Rand fault mylonite	309987	3861486	0	top E	270	SC
08SE236	Rand schist quartzite	322478	3862567	0	top W	67	SC
08SE340	Rand schist metasandstone	309912	3861283	0	coaxial	N/A	2SB
08SE631	Rand schist metasandstone	311720	3861700	−3	top E	306	SC
08SE241	Rand schist deformed quartz vein	322715	3862533	−14	top W	72	SC
08SE651	Rand schist metasandstone	311542	3861851	−21	top E	296	SC
06SE29	Rand schist quartzite	311187	3861844	−31	top E	315	QF, MF, SC
08SE210	Rand schist quartzite	322130	3862568	−31	top E	283	SC
06SE66	Rand schist quartzite mylonite	310749	3861869	−37	top E	275	QF, SC, MF
06SE37	Rand schist quartzite	314535	3862739	−247	top W	100	SC, AP
06SE35	Rand schist metasandstone	314607	3862477	−283	top E	263	SC, AP
08SE473	Rand schist quartzite mylonite	319423	3862435	−623	coaxial	N/A	QF, 2SB

[a]UTM coordinates are WGS datum, zone 11N.
[b]Distance to Rand fault: positive and negative values indicate position above and below the Rand fault, respectively.
[c]Shear sense criteria: AP, asymmetric porphyroclasts; SC, S-C fabric; 2SB, 2 sets of shear bands; MF, mica fish; QF, quartz fabrics (CPO).

the shear bands assume a conjugate form suggesting a strong coaxial component of shear strain. In a critical area (~20 x 30 m) in the proximal hanging wall of the schist half window, a top to the northeast shear sense is apparent in asymmetric leucotonalite boudins and associated lineation patterns. This shear sense is consistent with that of S-C fabrics, mica fish, asymmetric hornblende porphyroclasts, and asymmetric boudins in White Oak unit mylonites east of the half window [*Wood*, 1997] (Figure 8).

3.5. Deformation Temperature, Strain, and Flow Vorticity Analysis Using Quartz Fabrics

[22] For the case of homogeneous flow, the relative proportions of pure shear and simple shear can be derived by means of the kinematic vorticity number W_k. For steady state deformation, i.e., no spatial gradients in velocity, $W_k = \cos\theta$, where θ is the minimum angle between the two directions of zero angular velocity (the flow apophyses) [*Hanmer and Passchier*, 1991; *Wallis*, 1992, 1995]. In cases of nonsteady state flow, the finite deformation is more appropriately characterized by the space and time integrated mean vorticity number W_m [*Passchier*, 1988]. The likelihood of nonsteady state flow during progressive deformation is problematic for flow vorticity analysis; specifically, for a given analytical procedure, uncertainties exist as to whether the technique records time-integrated flow or the last few increments of deformation. However, recent vorticity studies indicate that differences in W_m from sample to sample can be detected with the use of the quartz c axis fabric and strain ratio method (abbreviated here as the R_{xz}/β method) [*Wallis*, 1992, 1995; *Grasemann et al.*, 1999; *Law et al.*, 2004; *Xypolias*, 2009]. In our vorticity analysis of the Rand schist, we apply this method to estimate the relative contributions of pure shear and simple shear at different structural levels.

[23] The R_{xz}/β method assumes steady state monoclinic flow symmetry and that the angle between the foliation (flattening plane of finite strain) and the normal to the central segment of the c axis girdle (shear plane), β, is dependent on finite strain and flow vorticity. Therefore, if β and the strain ratio in the XZ plane of finite strain (R_{xz}) are known, W_m can be calculated by [*Wallis*, 1992, 1995]

$$W_m = \sin\left[\tan^{-1}\left\{\frac{\sin 2\beta}{\frac{(R_{xz}+1)}{(R_{xz}-1)} - \cos 2\beta}\right\}\right]\frac{(R_{xz}+1)}{(R_{xz}-1)} \qquad (1)$$

To estimate R_{xz}, we used the R_f/ϕ method [*Ramsay*, 1967; *Dunnet and Siddans*, 1971; *Lisle*, 1985] by approximating detrital quartz grain shapes as ellipses and measuring the axial ratio (R_f) and orientation of the long axis with respect to the foliation (ϕ). Care was taken to avoid grains that were recrystallized, although it is possible that some small new grains were mistaken for larger original detrital grains. This is especially true for sample 06SE66, which has likely been significantly recrystallized and we interpret the calculated R_{xz}

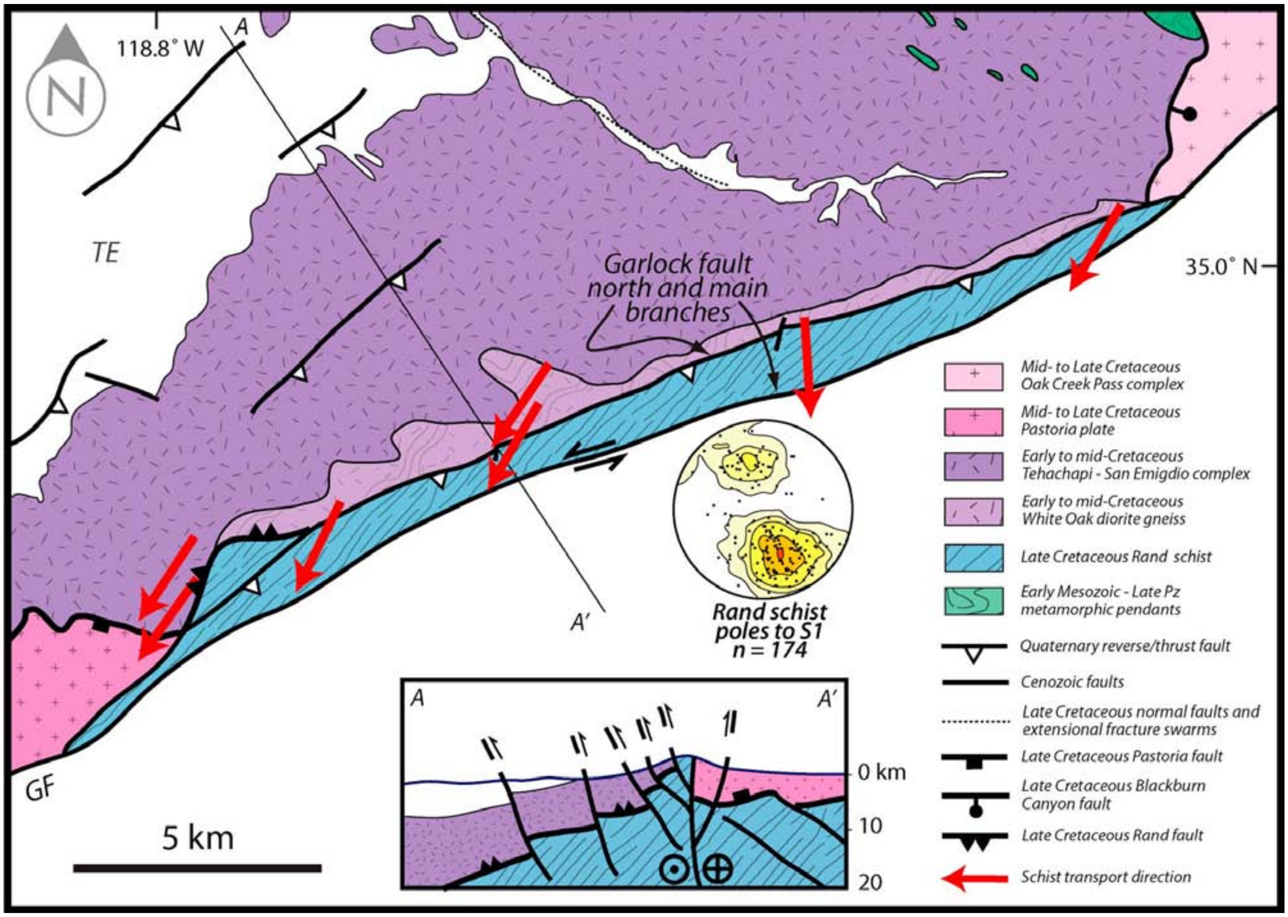

Figure 8. Simplified geologic map of the Tehachapi Mountains. Geology after [*Sharry* 1981], *Saleeby et al.* [1987; 2007], *Ross* [1989], *Wood* [1997], and this study. Generalized NNW–SSE cross section after [*Malin et al.*1995]. Schist foliation data are presented as an equal-area lower hemisphere stereographic projection of the orientation of poles to mylonitic foliation (S1) (Kamb contours at 2σ, 4σ, 6σ, 10σ, and 14σ) [*Sharry*, 1981]. All shear sense determinations from White Oak diorite gneiss. Abbreviations as in Figure 1.

value of 8.2 as a lower bound. In contrast, quartz grains in sample 08SE473 are commonly pinned by mica, inhibiting the migration of quartz grain boundaries. R_{xz} values were calculated using the Excel spreadsheet of *Chew* [2003]. Mean vorticity number values, R_f/ϕ method-derived strain ratios in the XZ plane of the finite strain ellipsoid, and measured angles between poles to foliation and the central segment of the c axis girdle are reported in Table 2. The range of W_m values reported for sample 08SE473 results from uncertainty in the measurement of β.

[24] We measured quartz crystallographic preferred orientation (CPO) from three oriented mylonitic quartzites collected from the San Emigdio schist locality by means of manual electron backscatter diffraction (EBSD) analyses (Figure 10). The locations of these samples are indicated on Figure 7. Samples 06SE66 and 06SE29 show strong fabrics with c axes populating type I girdles [*Lister*, 1977; *Schmid and Casey*, 1986]. The girdles are asymmetric in a top to the east sense and are oriented perpendicular to macroscopic shear bands with ⟨a⟩ directions aligned with the inferred

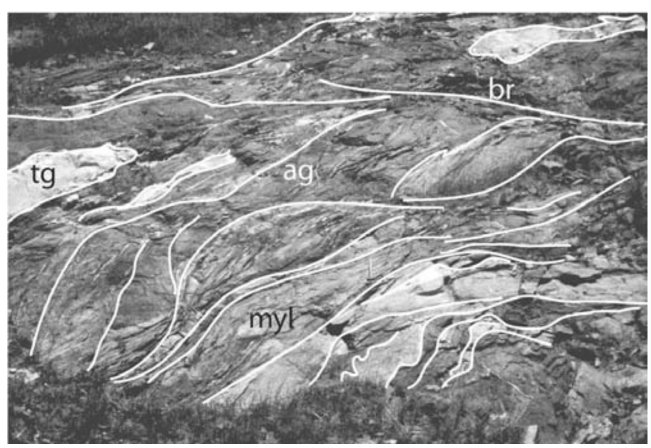

Figure 9. Photograph of highly attenuated White Oak diorite gneiss in the Tehachapi Mountains. Note anastomosing ductile to brittle shear bands between boudinaged dikes. Field of view 20 m long. Abbreviations ag, amphibolite gneiss; br, breccia; myl, mylonite; tg, tonalite gneiss.

Table 2. Summary of Quartz Fabric, Strain, and Vorticity Data From the San Emigdio and Rand Mountains

Sample	Locality[a]	Distance From Rand Fault (m)	Quartz c Axis Opening Angle	Deformation Temperature (°C)	Quartz c Axis β Angle	XZ Strain Ratio Rs	W_m[b]
06SE29	SE	31	66°	520 ± 50	17–21°	>5	A
06SE66	SE	37	63°	500 ± 50	6–8°	8.2	0.73–0.84
08SE473	SE	623	68°	540 ± 50	7–9°	3.2	0.48–0.59
309A	R	<100	65°	515 ± 50	15–22°	>5	A
309E-1	R	<100	67°	535 ± 50	9–11°	>5	A
301C	R	<100	65°	515 ± 50	11–12°	>5	A
524	R	<100	61°	480 ± 50	4–7°	>5	B
18	R	<100	-	-	13–19°	>5	A
14	R	<100	-	-	14–19°	>5	A
2	R	~500–700	73°	590 ± 50	7–9°	>5	B
9a	R	~750–1000	67°	535 ± 50	2–4°	>5	B
9b	R	~750–1000	60°	470 ± 50	3–7°	>5	B
9c	R	~750–1000	63°	500 ± 50	0–1°	>5	C
3b	R	~800–1000	-	-	0–1°	>5	C
40	R	~2500–4000	70°	550 ± 50	7–10°	>5	B

[a]SE, San Emigdio Mountains; R, Rand Mountains.
[b]Deformation settings [*Grasemann et al.*, 1999]: A, simple shear with $\beta > 10°$; B, general shear with intermediate β ($0° < \beta < 10°$); C, pure shear with $\beta \approx 0°$.

shear direction. This implies crystallographic slip along the basal plane in the ⟨a⟩ direction, a characteristic of noncoaxial greenschist facies deformation [*Schmid and Casey*, 1986]. Samples 06SE66 and 06SE29 contain elongate quartz ribbons that exhibit sweeping undulose extinction with recrystallized subgrain mantles (Figure 5g). These features are indicative of regime 2 (i.e., roughly greenschist facies conditions) quartz recrystallization [*Hirth and Tullis*, 1992].

[25] Upper greenschist to amphibolite facies mylonites commonly show quartz c axis maxima oriented parallel with the foliation and normal to the lineation (i.e., the Y direction of the finite strain ellipsoid) [*Schmid and Casey*, 1986]. Quartz CPO from sample 08SE473 is transitional between girdle-type and Y-maximum-type c axis fabrics, suggesting slightly higher deformation temperatures than 06SE66 (Figure 10). Conjugate sets of mica rich shear bands are locally developed, indicating a significant component of coaxial deformation. As in 06SE66, the ⟨a⟩ direction is aligned with the inferred shear direction; however, in addition to slip on the basal plane, slip is also accommodated on first order prism and both positive and negative rhomb planes. Evidence for both grain boundary migration and subgrain rotation in quartz implies transitional regime 2 to regime 3 recrystallization conditions [*Hirth and Tullis*, 1992] (Figure 5h). Quartz c axis fabric opening angles of 63°, 66°, and 68° (samples 06SE66, 06SE29, and 08SE473, respectively) indicate deformation temperatures of ~500°C [*Kruhl*, 1998; *Law et al.*, 2004] (Table 2). Similar opening angles (60°–73°) were observed in samples from the Rand Mountains, discussed below, indicating similar conditions of deformation. Systematic variations in opening angle with structural depth were not observed in either San Emigdio or Rand localities, implying that the entire structural section of schist was deformed at ~500°C.

[26] Quartz CPO for 12 samples of Rand schist quartzite mylonite from different structural levels in the Rand Mountains are compiled from *Postlethwaite and Jacobson* [1987] and *Nourse* [1989] and shown in Figure 11. For samples collected from the upper ~100 m of the schist, a systematic obliquity exists between the central portion of c axis fabrics and the foliation, consistent with TTN shear. At deeper structural levels (>100 m from the Rand fault), c axis fabrics are more symmetric about the foliation, indicating a stronger influence of coaxial flow.

[27] Near the schist–upper plate contact, quartz ribbon microstructures are well preserved in strongly lineated and foliated tectonites with individual ribbon aspect ratios > 20:1 [*Nourse*, 1989]. Estimates of finite strain near the base of the schist section from deformed volcanic "clasts" indicate highly flattening strain with strain ellipsoid axial ratios of 1.5:1.0:0.1 and $R_{xz} = 16.3 \pm 1.4$ [*Postlethwaite*, 1983]. At this level of exposure, lineations are poorly developed and boudinage of quartzite layers is common [*Postlethwaite*, 1983]. Strain estimates were not possible for the samples presented in Figure 11 or for sample 06SE29 due to difficulties in recognizing and tracing outlines of detrital quartz grains. However, given the high strains ($R_{xz} > 16$) observed at different structural levels by *Postlethwaite* [1983] and *Nourse* [1989] and the large displacement along the Rand fault (hundreds of kilometers), we assume large finite strains ($R_{xz} > 5$) for these samples. At high finite strain, vorticity number estimates are quite sensitive to small changes in β (Figure 12) and only three deformation settings can be distinguished: (1) pure shear with $\beta \approx 0°$; (2) general shear with intermediate β ($0° < \beta < 10°$); and (3) simple shear with $\beta > 10°$ [*Grasemann et al.*, 1999]. Measured β angles are summarized in Table 2. The highest values of β, averaging ~13° for samples 309A, 309E-1, 301C, 524, 18, and 14, are found within ~100 m of the Rand fault, indicating predominantly simple shear at high structural levels. In contrast, at deeper structural levels β averages ~4° (samples 2, 9a–c, 3b, and 40), implying a decrease in W_m (i.e., an increase in pure shear component) away from the Rand fault (Figure 12). Although we assume $R_{xz} > 5$ for the entire structural thickness of schist in the Rand Mountains, we consider it likely, based on larger strain estimates near the Rand fault [*Nourse*, 1989] than from deep in the section [*Postlethwaite*, 1983] and from strain analysis in the San Emigdio window ($R_{xz} > 8.2$ in

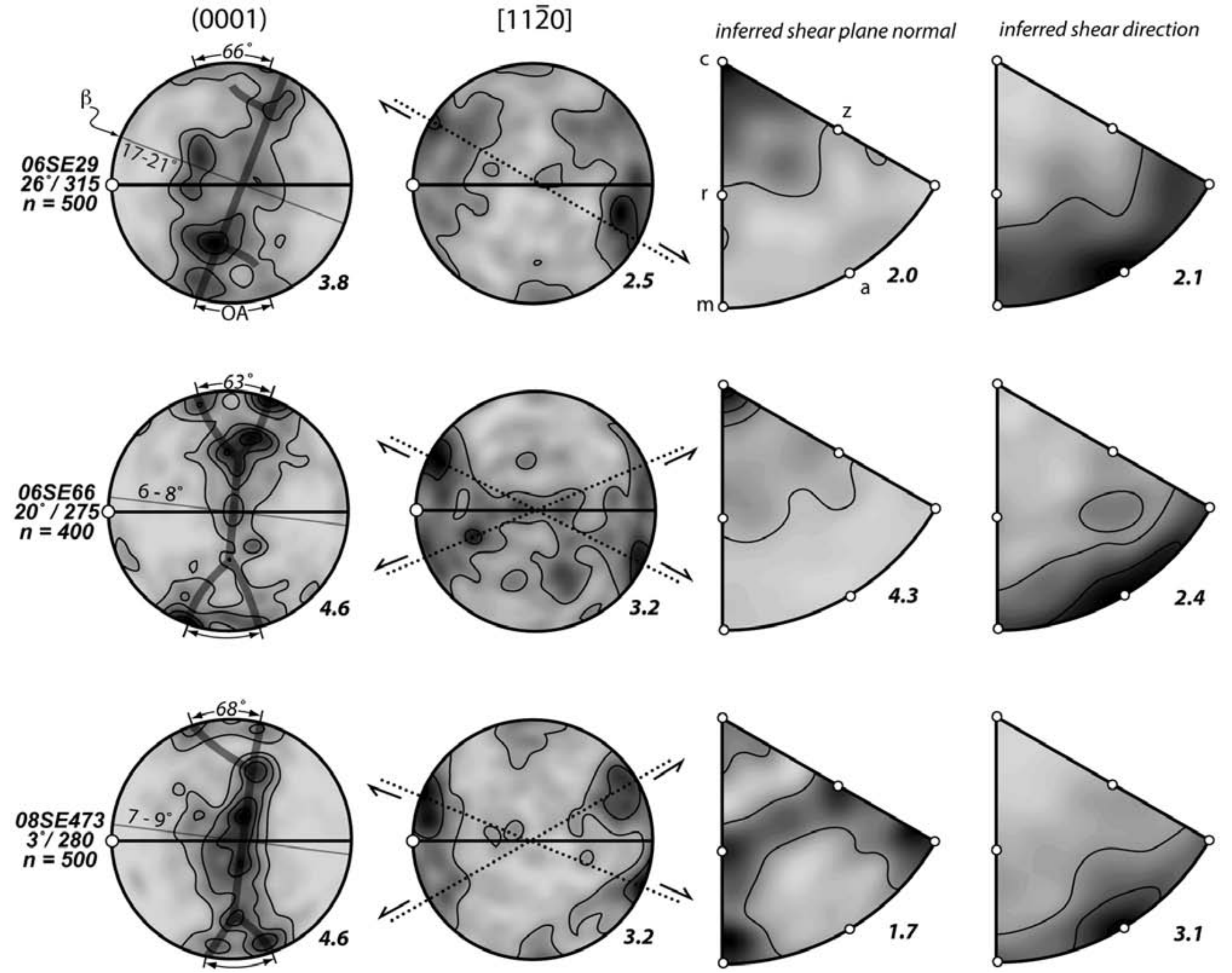

Figure 10. EBSD results showing quartz CPO. Pole figures are equal-area lower hemisphere stereographic projections (contours at 1, 2, 3, 4 times mean uniform distribution with maximum density shown under each figure) of c axes (0001) and second-order prisms [11$\bar{2}$0]; foliation shown by horizontal line, down-plunge lineation trend shown by white circle, average shear band orientation indicated by dashed line, skeletal outlines showing β of c axis fabric are overlain, and c axis fabric opening angles (OA) are shown for each sample. Inverse pole figures are for the inferred shear plane normal and the inferred direction of shear; c, basal plane; m, prism planes; a, second-order prism planes; r and z, positive and negative rhomb planes. Sample locations shown in Figure 7.

06SE66 and $R_{xz} \sim 3.2$ in 08SE473), that finite strain decreases with structural depth in the schist. A decrease in R_{xz} from the top of the schist downward would still require a decrease in W_m away from the Rand fault, although this scenario would involve a larger decrease than for the case of constant R_{xz} (Figure 12).

4. Discussion

4.1. Tectonic Model

[28] The deposition, subduction, and structural ascent of the schist is temporally and spatially associated in plate reconstructions with the subduction of a conjugate massif to the Shatsky Rise, a large igneous province (LIP) ~2000 km southeast of Japan [*Saleeby*, 2003; *Liu et al.*, 2008, 2010]. Subduction of the LIP is hypothesized to have driven slab flattening and upper plate extension (Figure 13) somewhat analogous to the ongoing subduction of the Nazca Ridge and trench-directed detachment faulting above the Peruvian flat slab segment [*Gutscher et al.*, 2000; *McNulty and Farber*, 2002]. To explain northwest–southeast younging patterns in protolith and cooling age of the schist [*Grove et al.*, 2003], we view this conjugate LIP as an elongate body that first collided with North America at the latitude of the San Emigdio Mountains and propagated to the southeast [*Barth and Schneiderman*, 1996]. As a result of this time-transgressive collision the events described below for the Tehachapi and San Emigdio windows occurred ~20 Myr prior to analogous

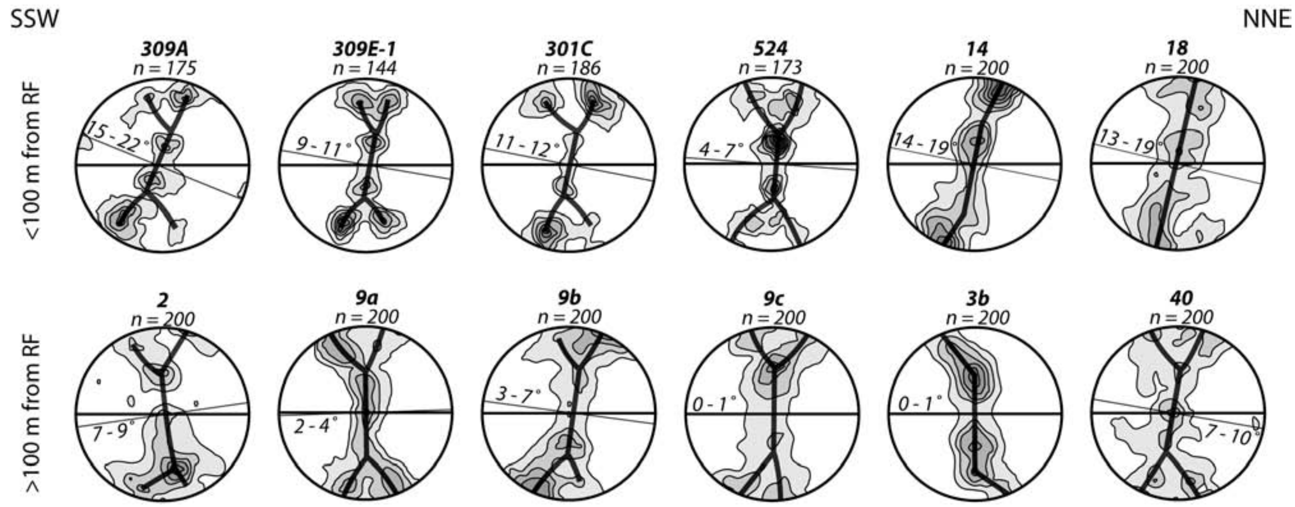

Figure 11. Quartz c axis fabrics for 12 samples of Rand schist quartzite mylonite from the Rand Mountains. Pole figures are equal-area lower hemisphere stereographic projections with foliation shown by horizontal line and lineation parallel to the projection plane (oriented NNE–SSW), skeletal outlines showing β of c axis fabric are overlain. Note higher β values and more systematic asymmetry of the central portion of c axis fabrics proximal to Rand fault (RF). Samples 309A, 309E-1, 301C, and 524 from *Nourse* [1989], contouring at 1, 3, 5, 7, 9, 11, and 13 times mean uniform distribution. Samples 14, 18, 2, 9a–c, 3b, and 40 from *Postlethwaite and Jacobson* [1987], Kamb contours at 2σ, 4σ, 6σ, 8σ, 10σ, and 12σ. Sample locations shown in Figure 3.

events in the Sierra de Salinas and the Rand Mountains. At circa 95 Ma (Figure 13b), the LIP entered the trench with a high normal component of convergence (~100 km/Myr) [*Engebretson et al.*, 1985] and the angle of subduction shallowed, driving the tectonic removal of subbatholithic mantle lithosphere and the cessation of arc magmatism. Increased coupling between the LIP and the upper plate led to abrupt crustal thickening [*House et al.*, 2001; *Saleeby*, 2003]. Decompression and partial exhumation of batholithic assemblages from ~9 to ~4 kbar levels occurred during this phase of rapid uplift. Erosion of the high-elevation mountain belt shed the schist protolith into the trench, which was immediately underplated and subjected to high-temperature metamorphism at least 150 km inboard beneath the recently extinguished arc [*Kidder and Ducea*, 2006]. Replacement of subbatholith mantle lithosphere with relatively weak schist led to gravitational collapse of the thickened upper plate and regionally extensive trench-directed flow in the schist [*Saleeby*, 2003]. During this exhumation phase, (1) the KWF functioned as a crustal-scale transfer structure, the southeastern side of which underwent high-magnitude extension and clockwise rotation above the trenchward-moving schist (Figure 13c) and (2) northwest striking extensional fracture swarms southeast of the KWF (Figures 1 and 13c) developed perpendicular to the principal transport direction in the underplated schist.

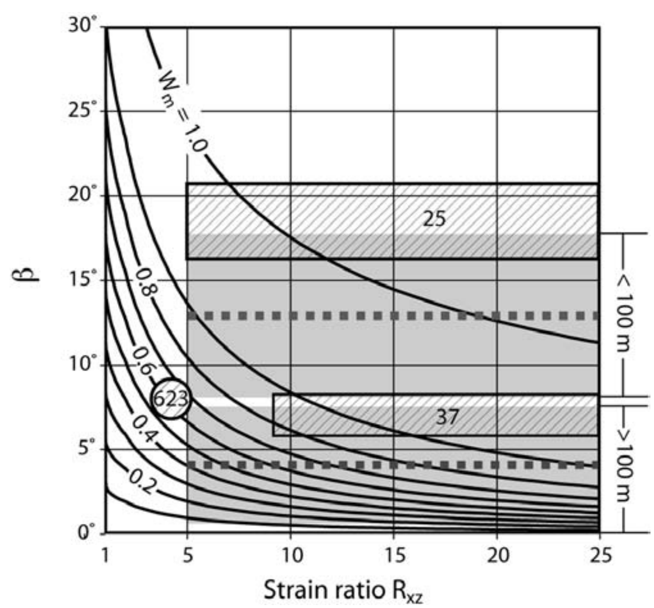

Figure 12. Relationship between R_{xz} and β for different values of W_m. Vorticity constraints from the San Emigdio schist locality are shown as boxes (06SE66 and 06SE29) and a circle (08SE473) with hachured lines and distance from the Rand fault (in meters) inscribed. For the Rand locality, average β (dashed dark gray lines) and standard deviation envelopes (gray boxes) are shown for $R_{xz} > 5$ for <00 m and >100 m from the Rand fault (see text for discussion).

4.2. Rotation of the Southern Sierra Nevada Batholith

[29] The structural and kinematic relations presented here provide strong evidence that the schist moved from deep to shallow crustal levels along the Rand fault and Salinas shear

zone with a top to the NNE sense of shear. With the exception of the San Emigdio Mountains, which experienced significant Pliocene-Quaternary contractile deformation [*Davis*, 1983], lower plate transport directions are uniform at S30W ± 10° within a ~10,000 km^2 region (Figure 1). The consistency in schist transport direction stands in marked contrast to apparent vertical axis rotations of 45–90° [*Kanter and McWilliams*, 1982; *McWilliams and Li*, 1983, 1985] observed in the batholithic rocks from the same region, and suggests that the schist escaped major systematic rotation. It could be argued that the Garlock fault may be a transrotation boundary [e.g., *Dickinson*, 1996] and that any rotation in the southern Sierra Nevada (e.g., in the Tehachapi schist body) would not be expected in the Sierra de Salinas or Rand windows. However, the geometry and kinematics of Neogene-Quaternary faulting in the southern Sierra Nevada are inconsistent with the proposed boundary [*Mahéo et al.*, 2009].

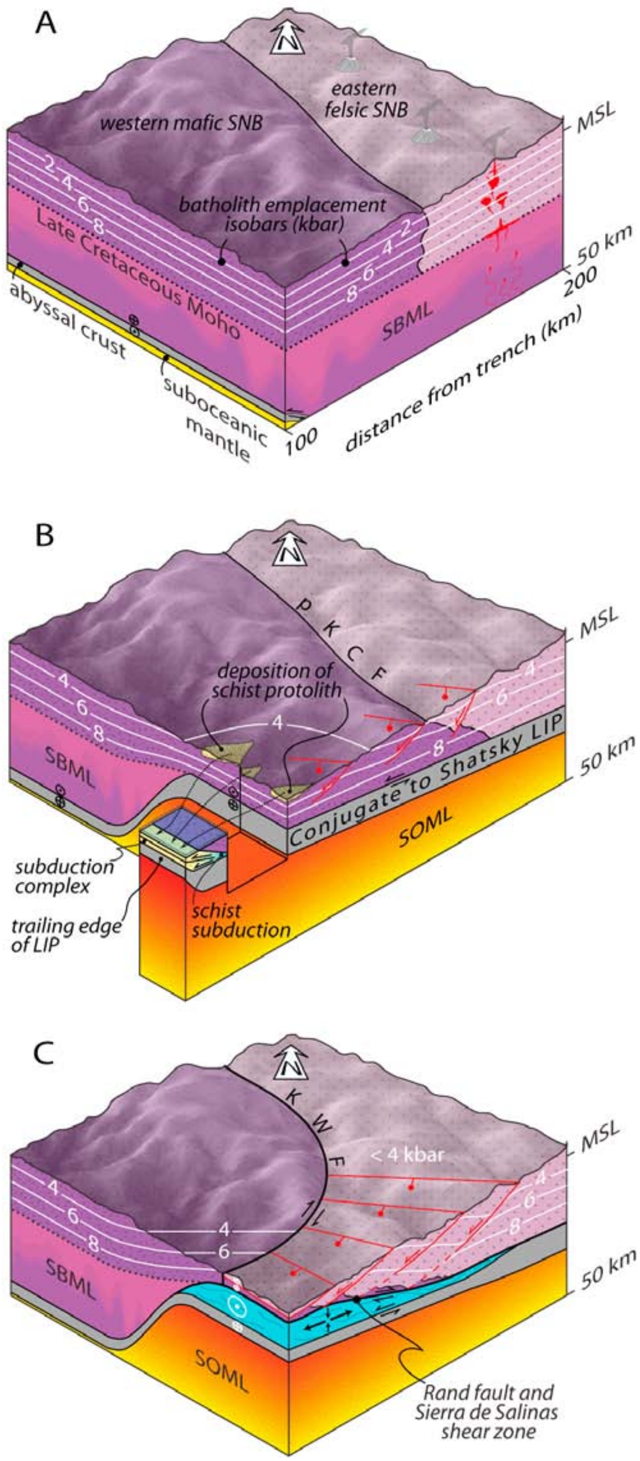

[30] In the SNB, circa 86 Ma $^{40}Ar/^{39}Ar$ cooling ages indicate that the schist reached its present position relative to the upper plate at about the same time that the upper plate cooled sufficiently to lock in a magnetic orientation (circa 88–80 Ma). These observations leave little time for rotation prior to schist arrival, and rule out major crustal block rotation following circa 86 Ma. We assume that following schist emplacement and cooling, any upper plate rotation that occurred would also involve rotation of the underlying schist. We conclude that a significant fraction of upper plate rotation of the southern SNB occurred in the Late Cretaceous coincident with schist ascent and cooling at circa 88–86 Ma. It is important to reiterate here that fabrics at the base of the upper plate and in the schist are generally parallel. We suggest that the trenchward flowing schist exerted traction at the base of the upper plate, driving upper plate extension and rotation. We further speculate that this coupling increased toward the Rand fault (i.e., from high to low structural levels in the upper plate), leading to the observed upper plate clockwise deflection into parallelism with the schist. This interpretation is at odds with models linking clockwise rotation in the southern SNB to post-Cretaceous dextral transpression [*Burchfiel and Davis*, 1981; *McWilliams and Li*, 1985] or Miocene transtension [*Ross et al.*, 1989; *Dokka and Ross*, 1995]. Although the west directed thrusting model of *May*

Figure 13. Block diagrams of the southern SNB showing the tectonic context of northward tilting and westward deflection of the upper plate and the development of lower plate transport directions. (a) Circa 100 Ma. Immediately prior to collision of the LIP. (b) Circa 95 Ma. Segmentation of the Farallon slab into shallow and more deeply subducting portions, with intervening lateral ramp. To the north, the subbatholith mantle lithosphere is preserved, while to the south, the mantle wedge is sheared off by the subducting LIP. Schist protolith is shed into trench and begins to subduct while upper plate uplift and extensional collapse occur above the shallow segment. (c) Circa 85 Ma. Gravitational collapse of the upper plate drives trench-directed channelized extrusion of the schist. Strain coupling between the schist and upper plate leads to continued extension and exhumation in the upper plate, and clockwise rotation in the upper plate. Schist flow is dominated by simple shear near the boundaries of the channel and by pure shear at the center of the wedge. Abbreviations KWF, Late Cretaceous Kern Canyon–White Wolf fault system; LIP, large igneous province; MSL, mean sea level; pKCF, proto-Kern Canyon fault; SBML, subbatholith mantle lithosphere; SOML, suboceanic mantle lithosphere.

[1989] attributes displacement of upper crustal fragments in the southern SNB, Salinia, Mojave Desert, Transverse Ranges, and Peninsular Ranges to Late Cretaceous deformation, the tectonic setting of the deformation is demonstrably extensional [*Wood and Saleeby*, 1997; *Saleeby et al.*, 2007].

4.3. Schist Exhumation Mechanisms

[31] Previous workers have proposed a number of scenarios for exhumation of the schist, both for the northern schist that we focus on here and for related Pelona and Orocopia schists to the south [e.g., *Grove et al.*, 2003]: return flow [*Malin et al.*, 1995; *Oyarzabal et al.*, 1997; *Jacobson et al.*, 2002; *Saleeby*, 2003; *Saleeby et al.*, 2007], isostatically driven uplift [*Jacobson et al.*, 2007], upper plate normal faulting [e.g., *Jacobson et al.*, 1996] and erosion [*Yin*, 2002]. Upper plate ductile thinning [e.g., *Ring et al.*, 1999] was apparently not a major schist exhumation mechanism since the upper plate is rather heterogeneously deformed. As the distinction between return flow and extrusion may not be clear, we first define these terms as end-member possibilities in what we recognize in nature may be a continuum of scenarios.

[32] We consider "return flow" in the sense of *Cloos* [1982]: forced convection of low viscosity material above a downgoing plate with zero- or low-slip boundary conditions. In return flow, subducted material returns to the surface along roughly the same route as it descended [*Platt*, 1986]. Return flow involves concurrent downward and upward flow resulting in a distributed, strongly noncoaxial flow. Return flow is extended from the steady state scenario of *Cloos* [1982] in the numerical models of *Gerya et al.* [2002], which illustrate the growth of a return flow channel over time.

[33] In the context of subducted material, extrusion, like return flow, involves the channelized structural ascent of material along roughly the same path as it descended. In the case of extrusion, exhumation occurs by localization of noncoaxial flow along coeval upper and lower shear zones with opposing senses of shear. Unlike the return flow "two-way street," the extrusion end-member brings the entire subduction assemblage toward the trench en masse. The resulting flow pattern is predominantly coaxial except near the boundaries of the channel. Strain compatibility is maintained during extrusion by discontinuous deformation along channel boundaries and elongation at the center of the wedge.

[34] Retrograde deformation features in the schist are more consistent with channelized extrusion than return flow. Microstructural observations from the Sierra de Salinas also suggest generally coaxial deformation in lower levels of the schist (Figure 6). These observations are inconsistent with distributed TTN noncoaxial flow as predicted within a return flow channel. We assert that the predominant exhumation mechanism of the schist was extrusion, i.e., deformation in the interior of the schist was predominantly coaxial with coeval noncoaxial shear displacement limited to the remobilized subduction megathrust and an unexposed structure with opposing shear sense at depth (Figure 13c). This general shear extrusion involves more rapid lower plate schist ascent than would be expected for the case of strictly noncoaxial deformation [*Grasemann, et al.*, 1999; *Law et al.*, 2004] and is consistent with high decompression rates of >0.5 kbar/Myr (>1.5 mm/yr) in the schist [*Saleeby et al.*, 2007]. Comparable decompression rates of ~2–4 mm/yr are calculated from the High Himalayan Crystalline Series [*Ganguly et al.*, 2000; *Searle et al.*, 2003; *Harris et al.*, 2004], which is suggested to have been exhumed by extrusion from beneath the Tibetan Plateau [e.g., *Burchfiel and Royden*, 1985; *Grujic et al.*, 1996; *Grasemann et al.*, 1999; *Hodges et al.*, 2001; *Law et al.*, 2004].

[35] Extrusion and return flow, acting alone or in combination, return subducted material to the surface at the trench rather than substantially inboard beneath the magmatic arc where the schists are found. Some combination of upper plate normal faulting and erosion thus played an important role in schist exhumation [*Postlethwaite and Jacobson*, 1987; *Jacobson et al.*, 1988, 1996; *Simpson*, 1990; *Malin et al.*, 1995; *Wood and Saleeby*, 1997; *Jacobson et al.*, 2007; *Saleeby et al.*, 2007]. Extensive upper plate normal faulting is evident from the regional displacement pattern of the extended southern SNB and the outboard position of Salinia. We speculate that the dominant exhumation mechanism evolved from extrusion in the middle and lower crust to extensional faulting and erosion in the upper crust.

[36] A critical assumption, supported by the following arguments, of the interpretation that the schist ascended by channelized extrusion is that coaxial and noncoaxial fabrics developed at the same time.

[37] 1. Deep and shallow fabrics in the Rand, San Emigdio, and Tehachapi bodies are commonly associated with retrograde mineral assemblages.

[38] 2. Amphibolite facies mylonites from the Sierra de Salinas indicate a high probability of noncoaxial flow at the top of the schist and the base of the upper plate, while at deeper levels (>200 m) TTN and TTS shear indicators are roughly evenly distributed (Figure 6). These "early" features, while commonly overprinted by demonstrably retrograde "late" fabrics, probably record exhumation-related deformation since the TTN sense of shear at the top of the schist is opposite the subduction direction. This is not the case, however, in the Orocopia schist, in which two generations of deformation are attributed to subduction and exhumation [*Jacobson and Dawson*, 1995; *Jacobson et al.*, 2007].

[39] 3. In the Rand and San Emigdio Mountains, quartz CPO indicate that plastic deformation occurred by localized simple shear-dominated deformation proximal to the upper plate at the same temperature conditions (~500°C) as more coaxial deformation in deeper parts of the schist. Inverted gradients preserved in the schist likely formed during prograde metamorphism [e.g., *Kidder and Ducea*, 2006]; therefore, since the entire schist section was deformed at ~500°C, this deformation must have occurred following peak metamorphism.

[40] 4. While peak metamorphic temperatures in the Rand Mountains window of 525–556°C [*Graham and Powell*, 1984] are similar to deformation temperatures of 470–590°C inferred from quartz fabrics (Table 2), peak temperatures in the Tehachapi and San Emigdio Mountains of 590–680°C [*Pickett and Saleeby*, 1993] are significantly higher, indi-

cating that these fabrics could not have formed prior to peak metamorphism (i.e., during underthrusting).

4.4. A Comparison With Cordilleran Metamorphic Core Complexes

[41] Like the schist–upper plate system, middle Tertiary metamorphic core complexes of the North American Cordillera formed as predominantly brittle upper crust extended by normal faulting above a weak substrate [*Coney*, 1980]. A detailed comparison of the schist and Cordilleran metamorphic core complexes has been made previously [*Jacobson et al.*, 2007] and is beyond the scope of this paper. We note, however, one key difference between the schist and core complexes. Schist exhumation involved lower plate transport to the SSW in at least Sierra de Salinas, Tehachapi, Rand, Orocopia, and Gavilan Hills localities [*Simpson*, 1990; *Jacobson et al.*, 1996; *Oyarzabal et al.*, 1997] (Figure 1 bottom inset), i.e., in each locality where a sense of shear has been established. In contrast, Cordilleran core complexes show no systematic sense of shear [*Wernicke*, 1992, Plate 8]. For example, the Shuswap core complex of the Canadian Cordillera crops out over an area comparable to that of the schist and exhibits opposing shear sense along its western (top to the west) and eastern (top to the east) margins [*Vanderhaeghe et al.*, 1999]. The consistency of schist transport to the SSW highlights the role of the schist as an active agent of tectonic rotation and large magnitude extension in the upper plate. In core complexes, the middle crust flows more passively in response to the local asymmetries of breakaway zones, forming domes beneath brittlely thinned upper crust [*Wernicke*, 1992].

4.5. Do the Schist Localities Preserve a Subduction Interface?

[42] Metamorphic convergence between an upper and lower plate of a subduction zone may result through either prograde metamorphism in the lower plate and retrograde metamorphism in the upper plate or retrograde metamorphism in both plates. The former type of metamorphic convergence along the schist–upper plate contact is cited as evidence for localized preservation of the original subduction interface [*Jacobson et al.*, 1996; *Jacobson*, 1997]. While we do not dispute this claim for the case of the Pelona schist of the San Gabriel Mountains, where no consistent direction of transport has been established [*Jacobson*, 1983; *Dillon et al.*, 1990], metamorphic convergence in the northern schists is at odds with the observed top to the NNE transport direction. We suggest that the contact was indeed proximal to the original subduction megathrust, but was later remobilized as a normal fault during exhumation. The current upper–lower plate configuration may have resulted from upper plate decompression to ~4 kbar conditions at the time of schist subduction to ~9 kbar conditions [*Saleeby et al.*, 2007]. Subsequent schist extrusion would have placed the schist against an upper plate that had already been exhumed from deep levels. In other words, metamorphic convergence along the Rand fault and Salinas shear zone may be a structural accident. Further thermochronologic work is needed to verify this hypothesis since it is based on upper plate and schist cooling ages from Tehachapi and San Emigdio localities, respectively [*Saleeby et al.*, 2007]. It is also possible that the schist–upper plate contact fused at peak conditions resulting in a low-slip boundary that is still preserved. In either case, while the shear zones involving Pelona, Orocopia, Rand, and Sierra de Salinas schists preserve metamorphic and structural evidence for deformation along the Late Cretaceous subduction megathrust, they subsequently experienced a significant penetrative, exhumation-related deformation. Deciphering prograde deformation through retrograde overprints remains a significant challenge for studies relating metamorphic and microstructural observations to subduction megathrust processes [e.g., *Peacock*, 1987; *England and Molnar*, 1993; *Ducea et al.*, 2007].

4.6. Dynamics of Schist Exhumation

[43] One outstanding geodynamic problem not resolved here is whether schist unroofing and associated collapse of the overthickened upper plate were purely driven by excess potential energy or if extension was facilitated by slab rollback. *Saleeby* [2003] argues that following passage of a conjugate to the Shatsky rise, the slab became negatively buoyant and reverted to a steeper trajectory (i.e., slab rollback), inducing regionally extensive trench-directed flow in the underplated schist and coupled extensional collapse of the upper plate. Our studies do not elucidate the role of slab rollback in crustal structures. Further iterative studies between observational geophysics, geologic data, and dynamic modeling are needed to resolve this issue. Future generation three-dimensional modeling is required to investigate the slab rollback hypothesis by allowing lateral inflow of asthenosphere into steepening flat segments from regions above adjacent steeply dipping segments.

4.7. Late Cretaceous Regional Cooling

[44] Late Cretaceous extension in the western United States was not restricted to the southern Sierra Nevada region. Widespread Late Cretaceous cooling in the Mojave Desert region has long been recognized [e.g., *Dumitru et al.*, 1991]. *Wells et al.* [2005] link this cooling to extension by detailing the geometry, kinematics, deformation temperature, and thermal history of the Pinto shear zone in the New York Mountains (Figure 1 bottom inset). Similarly, synextensional emplacement of Late Cretaceous granites and pegmatites from the Iron, Old Woman, and Granite Mountains (Figure 1 bottom inset) indicates widespread Late Cretaceous approximately northeast–southwest extension in the eastern Mojave Desert region [*Wells and Hoisch*, 2008]. Late Cretaceous–early Tertiary extension in the western Mojave, Salinia, and the southern SNB is clearly linked to emplacement of Rand and related schists. However, *Wells and Hoisch* [2008] suggest that synconvergent extension and magmatism in the eastern Mojave Desert region resulted from delamination of mantle lithosphere in the back-arc region, causing asthenospheric upwelling and partial melting in the lower crust. Recent work by *Luffi et al.* [2009] shows that the cratonic basement of the eastern Mojave Desert region is underlain by a section of North American lithospheric mantle above tectonically imbricated Farallon oceanic lithosphere.

The presence of North American lithospheric mantle beneath the Mojave Desert region precludes complete removal of Mojavian lithospheric mantle in the back-arc region due to delamination. Instead, we suggest that schist extrusion and arc collapse to the west enabled extension, asthenospheric upwelling, and anatexis in the eastern Mojave by changing plate boundary conditions. In other words, following passage of the LIP, gravitational collapse of the rootless SNB to the west pulled the more rigid crust of the eastern Mojave with it, allowing for asthenospheric upwelling and synextensional magmatism. This localized phenomenon may explain focused Late Cretaceous extension in the Mojave with considerably less extension at this time in other parts of the Cordillera [*Wells and Hoisch*, 2008].

5. Conclusions

[45] Through consideration of new and published structural data, recent geochronologic studies, and available paleomagnetic constraints, we have developed a model for roughly coeval high magnitude extension, clockwise rotation, and schist extrusion in Salinia and the southern SNB. We suggest the following sequence of Late Cretaceous events in the southern SNB and Salinia: (1) low angle subduction of a conjugate to the Shatsky Rise, resulting in uplift of the upper plate and schist underplating; (2) trench-directed channelized extrusion in the subducted schist with lower plate to the SSW kinematics, leading to collapse of the upper plate; and (3) high magnitude extension and westward deflection of the upper plate batholith above the flowing channel. We argue that a significant fraction of observed clockwise rotation in the southern SNB is the direct result of schist return flow; this argument does not preclude localized, basement structure-controlled, increments of Neogene rotation.

[46] **Acknowledgments.** This research was supported by National Science Foundation grant EAR-0739071. This is Caltech Tectonics Observatory Contribution 129. We thank Marty Grove, Peter Luffi, and Elisabeth Nadin for discussions. The manuscript benefited from thoughtful reviews by Carl Jacobson and Robert Miller. We thank Ralf Hielscher for providing quantitative texture analysis software, MTEX for processing EBSD data. We also thank Rick Allmendinger for use of Stereonet 1.2.0.

References

Ague, J. J., and G. H. Brimhall (1988), Magmatic arc asymmetry and distribution of anomalous plutonic belts in the batholiths of California: Effects of assimilation, crustal thickness, and depth of crystallization, *Geol. Soc. Am. Bull.*, *100*, 912–927, doi:10.1130/0016-7606(1988)100<0912:MAAADO>2.3.CO;2.

Barth, A. P., and J. S. Schneiderman (1996), A comparison of structures in the Andean Orogen of northern Chile and exhumed midcrustal structures in southern California, USA: An analogy in tectonic style?, *Int. Geol. Rev.*, *38*, 1075–1085, doi:10.1080/00206819709465383.

Barth, A. P., J. L. Wooden, M. Grove, C. E. Jacobson, and J. N. Pedrick (2003), U-Pb zircon geochronology of rocks in the Salinas Valley region of California: A reevaluation of the crustal structure and origin of the Salinian Block, *Geology*, *31*, 517–520, doi:10.1130/0091-7613(2003)031<0517:UZGORI>2.0.CO;2.

Burchfiel, B. C., and G. A. Davis (1981), Mojave Desert and environs, in *The Geotectonic Development of California, Rubey*, vol. I, edited by W. G. Ernst, pp. 217–252, Prentice-Hall, Englewood Cliffs, N. J.

Burchfiel, B. C., and L. H. Royden (1985), North-south extension within the convergent Himalayan region, *Geology*, *13*, 679–682, doi:10.1130/0091-7613(1985)13<679:NEWTCH>2.0.CO;2.

Cheadle, M. J., B. L. Czuchra, T. Byrne, C. J. Ando, J. E. Oliver, L. D. Brown, S. Kaufman, P. E. Malin, and R. A. Phinney (1986), The deep crustal structure of the Mojave Desert, California, from COCORP seismic reflection data, *Tectonics*, *5*, 293–320, doi:10.1029/TC005i002p00293.

Chew, D. M. (2003), An Excel spreadsheet for finite strain analysis using the R_f/ϕ technique, *Comput. Geosci.*, *29*, 795–799, doi:10.1016/S0098-3004(03)00027-X.

Cloos, M. (1982), Flow melanges: Numerical modeling and geologic constraints on their origin in the Franciscan subduction complex, California, *Geol. Soc. Am. Bull.*, *93*, 330–344, doi:10.1130/0016-7606(1982)93<330:FMNMAG>2.0.CO;2.

Coney, P. J. (1980), Cordilleran metamorphic core complexes: An overview, in *Cordilleran Metamorphic Core Complexes*, edited by M. D. Crittenden Jr., P. J. Coney, and G. H. Davis, *Mem. Geol. Soc. Am.*, 153, 7–31.

Crowell, J. C. (1952), Geology of the Lebec Quadrangle, California, *Spec. Rep. Calif. Div. Mines Geol.*, *24*, 1–24.

Davis, T. L. (1983), Late Cenozoic structure and tectonic history of the western "Big Bend" of the San Andreas Fault and adjacent San Emigdio Mountains, Ph.D. thesis, Univ. of Calif., Santa Barbara.

Dibblee, T. W., Jr. (1967), Areal geology of the western Mojave Desert, California, *U.S. Geol. Surv. Prof. Pap.*, *522*, 153 pp.

Dibblee, T. W., Jr. (1973), Geologic maps of the Santiago Creek, Eagle Rest Peak, Pleito Hills, Grapevine, and Pastoria Creek quadrangles, Kern County, California, *U.S. Geol. Surv. Open File Rep.*, *73-57*.

Dibblee, T. W., Jr. (1974), Geologic maps of the Monterey, Salinas, Gonzales, Point Sur, Jamesburg, Soledad and Junipero Serra 15′ quadrangles, Monterey County, California, *U.S. Geol. Surv. Open File Rep.*, *74-1021*.

Dibblee, T. W., Jr. (1986), Geology of the San Emigdio Mountains, California, in *Geologic Transect Across the Western Transverse Ranges*, *Field Trip Guideb.*, vol. 48, edited by T. L. Davis and J. S. Namson, pp. 1–10, Pac. Sect., Soc. of Econ. Paleontol. and Mineral., Bakersfield, Calif.

Dickinson, W. R. (1996), Kinematics of transrotational tectonism in the California Transverse Ranges and its contribution to cumulative slip along the San Andreas transform fault system, *Spec. Pap. Geol. Soc. Am.*, *305*, 46 pp., doi:10.1130/0-8137-2305-1.1.

Dillon, J. T., G. B. Haxel, R. M. Tosdal, G. B. Haxel, R. W. Simpson, and K. A. Howard (1990), Structural evidence for northeastward movement on the Chocolate Mountains Thrust, southeasternmost California, *J. Geophys. Res.*, *95*, 19,953–19,971, doi:10.1029/JB095iB12p19953.

Dokka, R. K., and T. M. Ross (1995), Collapse of southwestern North America and the evolution of early Miocene detachment faults, metamorphic core complexes, the Sierra Nevada orocline, and the San Andreas fault system, *Geology*, *23*, 1075–1078, doi:10.1130/0091-7613(1995)023<1075:COSNAA>2.3.CO;2.

Ducea, M. N., and J. B. Saleeby (1998), The age and origin of a thick mafic-ultramafic keel from beneath the Sierra Nevada Batholith, *Contrib. Mineral. Petrol.*, *133*, 169–185, doi:10.1007/s004100050445.

Ducea, M. N., J. Ganguly, E. J. Rosenberg, P. J. Patchett, W. Cheng, and C. Isachsen (2003), Sm-Nd dating of spatially controlled domains of garnet single crystals; a new method of high-temperature thermochronology, *Earth Planet. Sci. Lett.*, *213*, 31–42, doi:10.1016/S0012-821X(03)00298-X.

Ducea, M. N., S. Kidder, and J. T. Chesley (2007), A geologic window into a subduction megathrust, *Eos Trans. AGU*, *88*, 277, doi:10.1029/2007EO270001.

Ducea, M. N., S. Kidder, J. T. Chesley, and J. B. Saleeby (2009), Tectonic underplating of trench sediments beneath magmatic arcs: The central California example, *Int. Geol. Rev.*, *51*, 1–26, doi:10.1080/00206810802602767.

Dumitru, T. A., P. B. Gans, D. A. Foster, and E. L. Miller (1991), Refrigeration of the Western Cordilleran lithosphere during Laramide shallow-angle subduction, *Geology*, *19*, 1145–1148, doi:10.1130/0091-7613(1991)019<1145:ROTWCL>2.3.CO;2.

Dunnet, D., and A. W. B. Siddans (1971), Non-random sedimentary fabrics and their modification by strain, *Tectonophysics*, *12*, 307–325, doi:10.1016/0040-1951(71)90019-9.

Ehlig, P. L. (1958), The geology of the Mount Baldy region of the San Gabriel Mountains, California, Ph.D. thesis, 195 pp, Univ. of Calif., Los Angeles.

Ehlig, P. L. (1981), Origin and tectonic history of the basement terrane of the San Gabriel Mountains, central Transverse Ranges, in *The Geotectonic Development of California, Rubey*, vol. I, edited by W. G. Ernst, pp. 253–283, Prentice-Hall, Englewood Cliffs, N. J.

Engebretson, D. C., A. Cox, and R. G. Gordon (1985), Relative motions between oceanic and continental plates in the Pacific Basin, *Spec. Pap. Geol. Soc. Am.*, *206*, 59 pp.

England, P., and P. Molnar (1993), The interpretation of inverted metamorphic isograds using simple physical calculations, *Tectonics*, *12*, 145–158, doi:10.1029/92TC00850.

Fletcher, J. M., J. S. Miller, M. W. Martin, S. S. Boettcher, A. F. Glazner, and J. M. Bartley (2002), Cretaceous arc tectonism in the Mojave Block: Profound crustal modification that controlled subsequent tectonic regimes, in *Geologic Evolution of the Mojave Desert and Southwestern Basin and Range*, edited by A. F. Glazner, J. D. Walker, and J. M. Bartley, *Mem. Geol. Soc. Am.*, *195*, 131–149, doi:10.1130/0-8137-1195-9.131.

Ganguly, J., S. Dasgupta, W. Cheng, and S. Neogi (2000), Exhumation history of a section of the Sikkim Himalayas, India: Records in the metamorphic mineral equilibria and compositional zoning of garnet, *Earth Planet. Sci. Lett.*, *183*, 471–486, doi:10.1016/S0012-821X(00)00280-6.

Gerya, T. V., B. Stöckhert, and A. L. Perchuk (2002), Exhumation of high-pressure metamorphic rocks in a subduction channel: A numerical simulation, *Tectonics*, *21*(6), 1056, doi:10.1029/2002TC001406.

Graham, C. M., and P. C. England (1976), Thermal regimes and regional metamorphism in the vicinity of overthrust faults: An example of shear heating and inverted metamorphic zonation from southern California, *Earth Planet. Sci. Lett.*, *31*, 142–152, doi:10.1016/0012-821X(76)90105-9.

Graham, C. M., and R. Powell (1984), A garnet-hornblende geothermometer; calibration, testing, and application to the Pelona schist, southern California, *J. Metamorph. Geol.*, *2*, 13–31, doi:10.1111/j.1525-1314.1984.tb00282.x.

Grasemann, B., H. Fritz, and J.-C. Vannay (1999), Quantitative kinematic flow analysis from the Main Central Thrust Zone (northwest-Himalaya, India); Implications for a decelerating strain path and the extrusion of orogenic wedges, *J. Struct. Geol.*, *21*, 837–853, doi:10.1016/S0191-8141(99)00077-2.

Grove, M., C. E. Jacobson, A. P. Barth, and A. Vucic (2003), Temporal and spatial trends of Late Cretaceous-early Tertiary underplating Pelona and related schist beneath southern California and southwestern Arizona, in *Tectonic Evolution of Northwestern México and the Southwestern USA, edited by S. E. Johnson et al., Spec. Pap. Geol. Soc. Am.*, *374*, 381–406.

Grujic, D., M. Casey, C. Davidson, L. S. Hollister, R. Kuendig, T. L. Pavlis, and S. M. Schmid (1996), Ductile extrusion of the Higher Himalayan Crystalline in Bhutan: Evidence from quartz microfabrics, *Tectonophysics*, *260*, 21–43, doi:10.1016/0040-1951(96)00074-1.

Gutscher, M.-A., W. Spakman, H. Bijwaard, and E. R. Engdahl (2000), Geodynamics of flat subduction: Seismicity and tomographic constraints from the Andean margin, *Tectonics*, *19*, 814–833, doi:10.1029/1999TC001152.

Hanmer, S., and C. Passchier (1991), Shear-sense indicators: A review, *Pap. Geol. Surv. Can.*, *90-17*.

Harris, N. B. W., M. Caddick, J. Kosler, S. Goswami, D. Vance, and A. G. Tindle (2004), The pressure-temperature-time path of migmatites from the Sikkim Himalaya, *J. Metamorph. Geol.*, *22*, 249–264, doi:10.1111/j.1525-1314.2004.00511.x.

Haxel, G., and J. Dillon (1978), The Pelona-Orocopia schist and Vincent-Chocolate Mountain thrust system, southern California, in *Mesozoic Paleogeography of the western United States*, *Pac. Coast Paleogeogr. Symp.*, vol. 2, edited by D. G. Howell and K. A. McDougall, pp. 453–469, Pac. Sect., Soc. of Econ. Paleontol. and Mineral., Bakersfield, Calif.

Henry, D. J., and R. K. Dokka (1992), Metamorphic evolution of exhumed middle to lower crustal rocks in the Mojave extensional belt, southern California, USA, *J. Metamorph. Geol.*, *10*, 347–364, doi:10.1111/j.1525-1314.1992.tb00089.x.

Hirth, G., and J. Tullis (1992), Dislocation creep regimes in quartz aggregates, *J. Struct. Geol.*, *14*, 145–159, doi:10.1016/0191-8141(92)90053-Y.

Hodges, K. V., J. M. Hurtado, and K. X. Whipple (2001), Southward extrusion of Tibetan crust and its effect on Himalayan tectonics, *Tectonics*, *20*, 799–809, doi:10.1029/2001TC001281.

House, M. A., B. P. Wernicke, and K. A. Farley (2001), Paleo-geomorphology of the Sierra Nevada, California, from (U-Th)/He ages in apatite, *Am. J. Sci.*, *301*, 77–102, doi:10.2475/ajs.301.2.77.

Jacobson, C. E. (1983), Structural geology of the Pelona schist and Vincent Thrust, San Gabriel Mountains, California, *Geol. Soc. Am. Bull.*, *94*, 753–767, doi:10.1130/0016-7606(1983)94<753:SGOTPS>2.0.CO;2.

Jacobson, C. E. (1990), The $^{40}Ar/^{39}Ar$ geochronology of the Pelona schist and related rocks, southern California, *J. Geophys. Res.*, *95*, 509–528, doi:10.1029/JB095iB01p00509.

Jacobson, C. E. (1995), Qualitative thermobarometry of inverted metamorphism in the Pelona and Rand schists, southern California, using calciferous amphibole in mafic schist, *J. Metamorph. Geol.*, *13*, 79–92, doi:10.1111/j.1525-1314.1995.tb00206.x.

Jacobson, C. E. (1997), Metamorphic convergence of the upper and lower plates of the Vincent Thrust, San Gabriel Mountains, southern California, USA, *J. Metamorph. Geol.*, *15*, 155–165, doi:10.1111/j.1525-1314.1997.00009.x.

Jacobson, C. E., and M. R. Dawson (1995), Structural and metamorphic evolution of the Orocopia schist and related rocks, southern California: Evidence for late movement on the Orocopia fault, *Tectonics*, *14*, 933–944, doi:10.1029/95TC01446.

Jacobson, C. E., M. R. Dawson, and C. E. Postlethwaite (1988), Structure, metamorphism, and tectonic significance of the Pelona, Orocopia, and Rand schists, Southern California, in *Metamorphism and Crustal Evolution of the Western United States, Rubey Volume*, edited by W. G. Ernst, pp. 976–997, Prentice-Hall, Englewood Cliffs, N. J.

Jacobson, C. E., F. R. Oyarzabal, and G. B. Haxel (1996), Subduction and exhumation of the Pelona-Orocopia-Rand schists, southern California, *Geology*, *24*, 547–550, doi:10.1130/0091-7613(1996)024<0547:SAEOTP>2.3.CO;2.

Jacobson, C. E., M. Grove, M. M. Stamp, A. Vucic, F. R. Oyarzabal, G. B. Haxel, R. M. Tosdal, and D. R. Sherrod (2002), Exhumation history of the Orocopia schist and related rocks in the Gavilan Hills area of southeasternmost California, in *Contributions to Crustal Evolution of the Southwestern United States*, edited by A. Barth, *Spec. Pap. Geol. Soc. Am.*, 365, 129–154.

Jacobson, C. E., M. Grove, A. Vucic, J. N. Pedrick, and K. A. Ebert (2007), Exhumation of the Orocopia schist and associated rocks of southeastern California; relative roles of erosion, synsubduction tectonic denudation, and middle Cenozoic extension, in *Convergent Margin Terranes and Associated Regions: A Tribute to W.G. Ernst*, edited by M. Cloos et al., *Spec. Pap. Geol. Soc. Am.*, 419, 1–37.

James, E. W., D. L. Kimbrough, and J. M. Mattinson (1993), Evaluation of displacements of pre-Tertiary rocks on the northern San Andreas Fault using U-Pb zircon dating, initial Sr, and common Pb isotopic ratios, in *San Andreas Fault System; Displacement, Palinspastic Reconstruction, and Geologic Evolution*, edited by R. E. Powell, R. J. Weldon II, and J. C. Matti, *Mem. Geol. Soc. Am.*, *178*, 257–271.

Kanter, L. R., and M. O. McWilliams (1982), Rotation of the southernmost Sierra Nevada, California, *J. Geophys. Res.*, *87*, 3819–3830, doi:10.1029/JB087iB05p03819.

Kidder, S., and M. N. Ducea (2006), High temperatures and inverted metamorphism in the schist of Sierra de Salinas, California, *Earth Planet. Sci. Lett.*, *241*, 422–437, doi:10.1016/j.epsl.2005.11.037.

Kidder, S., M. Ducea, G. Gehrels, P. J. Patchett, and J. Vervoort (2003), Tectonic and magmatic development of the Salinian Coast Ridge Belt, California, *Tectonics*, *22*(5), 1058, doi:10.1029/2002TC001409.

Kistler, R. W., and D. E. Champion (2001), Rb-Sr whole-rock and mineral ages, K-Ar, $^{40}Ar/^{39}Ar$, and U-Pb mineral ages, and strontium, lead, neodymium, and oxygen isotopic compositions for granitic rocks from the Salinian Composite Terrane, California, *U.S. Geol. Surv. Open File Rep.*, *01-453*, 84 pp.

Kruhl, J. H. (1998), Prism- and basal-plane parallel subgrain boundaries in quartz: A microstructural geothermobarometer, Reply, *J. Metamorph. Geol.*, *16*, 142–146.

Law, R. D., M. P. Searle, and R. L. Simpson (2004), Strain, deformation temperatures and vorticity of flow at the top of the Greater Himalayan Slab, Everest Massif, Tibet, *J. Geol. Soc.*, *161*, 305–320, doi:10.1144/0016-764903-047.

Leventhal, J. A., M. R. Reid, A. Montana, and P. Holden (1995), Mesozoic invasion of crust by MORB-source asthenospheric magmas, U.S. Cordilleran interior, *Geology*, *23*, 399–402, doi:10.1130/0091-7613(1995)023<0399:MIOCBM>2.3.CO;2.

Li, Y.-G., T. L. Henyey, and L. T. Silver (1992), Aspects of the crustal structure of the western Mojave Desert, California, from seismic reflection and gravity data, *J. Geophys. Res.*, *97*, 8805–8816, doi:10.1029/91JB02119.

Lisle, R. J. (1985), *Geological Strain Analysis: A Manual for the R_f/ϕ Technique*, 99 pp., Pergamon, New York.

Lister, G. S. (1977), Discussion; crossed-girdle c-axis fabrics in quartzites plastically deformed by plane strain and progressive simple shear, *Tectonophysics*, *39*, 51–54, doi:10.1016/0040-1951(77)90087-7.

Lister, G. S., and A. W. Snoke (1984), S-C mylonites, *J. Struct. Geol.*, *6*, 617–638, doi:10.1016/0191-8141(84)90001-4.

Liu, L., S. Spasojevic, and M. Gurnis (2008), Reconstructing Farallon Plate subduction beneath North America back to the Late Cretaceous, *Science*, *322*, 934–938, doi:10.1126/science.1162921.

Liu, L., M. Gurnis, M. Seton, J. Saleeby, R. D. Müller, and J. M. Jackson (2010), The role of oceanic plateau subduction in the Laramide orogeny, *Nat. Geosci.*, doi:10.1038/ngeo829.

Luffi, P., J. B. Saleeby, C.-T. A. Lee, and M. N. Ducea (2009), Lithospheric mantle duplex beneath the central Mojave Desert revealed by xenoliths from Dish Hill, California, *J. Geophys. Res.*, *114*, B03202, doi:10.1029/2008JB005906.

Mahéo, G., J. Saleeby, Z. Saleeby, and K. A. Farley (2009), Tectonic control on southern Sierra Nevada topography, California, *Tectonics*, *28*, TC6006, doi:10.1029/2008TC002340.

Malin, P. E., E. D. Goodman, T. L. Henyey, Y. G. Li, D. A. Okaya, and J. B. Saleeby (1995), Significance of seismic reflections beneath a tilted exposure of deep continental crust, Tehachapi Mountains, California, *J. Geophys. Res.*, *100*, 2069–2087, doi:10.1029/94JB02127.

Mattinson, J. M. (1978), Age, origin, and thermal histories of some plutonic rocks from the Salinian Block of California, *Contrib. Mineral. Petrol.*, *67*, 233–245, doi:10.1007/BF00381451.

May, D. J. (1989), Late Cretaceous intra-arc thrusting in southern California, *Tectonics*, *8*, 1159–1173, doi:10.1029/TC008i006p01159.

McNulty, B., and D. Farber (2002), Active detachment faulting above the Peruvian flat slab, *Geology*, *30*, 567–570, doi:10.1130/0091-7613(2002)030<0567:ADFATP>2.0.CO;2.

McWilliams, M., and Y. Li (1983), A paleomagnetic test of the Sierran Orocline hypothesis, *Eos Trans. AGU*, *64*, 686.

McWilliams, M., and Y. Li (1985), Oroclinal bending of the southern Sierra Nevada Batholith, *Science*, *230*, 172–175, doi:10.1126/science.230.4722.172.

Miller, R. B., S. R. Paterson, S. M. DeBari, and D. L. Whitney (2000), North Cascades Cretaceous crustal section: Changing kinematics, rheology, metamorphism, pluton emplacement and petrogenesis from 0 to 40 km depth, in *Guidebook for Geological Field Trips in Southwestern British Columbia and Northern Washington*, edited by G. J. Woodsworth et al., pp. 229–278, Geol. Assoc. of Can., Vancouver, B. C.

Nadin, E. S., and J. B. Saleeby (2008), Disruption of regional primary structure of the Sierra Nevada Batholith by the Kern Canyon fault system, California, in *Ophiolites, Arcs, and Batholiths: A Tribute to Cliff Hopson*, edited by J. E. Wright and J. W. Shervais, *Spec. Pap. Geol. Soc. Am.*, *438*, 429–454.

Nadin, E. S., and J. Saleeby (2010), Quaternary reactivation of the Kern Canyon fault system, southern Sierra Nevada, California, *Geol. Soc. Am. Bull.*, *122*, 1671–1685, doi:10.1130/B30009.1.

Naeser, N. D., C. W. Naeser, and T. H. McCulloh (1990), Thermal history of rocks in southern San Joaquin Valley, California: Evidence from fission-track analysis, *AAPG Bull.*, *74*, 13–29.

Nourse, J. A. (1989), Geological evolution of two crustal scale shear zones; Part I, The Rand thrust complex, northwestern Mojave Desert, California; Part II, The Magdalena metamorphic core complex, north central Sonora, Mexico, Ph.D. thesis, Calif. Inst. of Technol., Pasadena.

Oyarzabal, F. R., C. E. Jacobson, and G. B. Haxel (1997), Extensional reactivation of the Chocolate Mountains subduction thrust in the Gavilan Hills of southeastern California, *Tectonics*, *16*, 650–661, doi:10.1029/97TC01415.

Passchier, C. W. (1988), Analysis of deformation paths in shear zones, *Geol. Rundsch.*, *77*, 309–318, doi:10.1007/BF01848692.

Passchier, C. W., and R. A. J. Trouw (2005), *Microtectonics*, 2nd ed., 366 pp., Springer, Berlin.

Peacock, S. M. (1987), Thermal effects of metamorphic fluids in subduction zones, *Geology*, *15*, 1057–1060, doi:10.1130/0091-7613(1987)15<1057:TEOMFI>2.0.CO;2.

Pennacchioni, G., G. Di Toro, and N. S. Mancktelow (2001), Strain-insensitive preferred orientation of porphyroclasts in Mont Mary mylonites, *J. Struct. Geol.*, *23*, 1281–1298, doi:10.1016/S0191-8141(00)00189-9.

Pickett, D. A., and J. B. Saleeby (1993), Thermobarometric constraints on the depth of exposure and conditions of plutonism and metamorphism at deep levels of the Sierra Nevada Batholith, Tehachapi Mountains, California, *J. Geophys. Res.*, *98*, 609–629, doi:10.1029/92JB01889.

Pickett, D. A., and J. B. Saleeby (1994), Nd, Sr, and Pb isotopic characteristics of Cretaceous intrusive rocks from deep levels of the Sierra Nevada Batholith, Tehachapi Mountains, California, *Contrib. Mineral. Petrol.*, *118*, 198–215, doi:10.1007/BF01052869.

Platt, J. P. (1986), Dynamics of orogenic wedges and the uplift of high-pressure metamorphic rocks, *Geol. Soc. Am. Bull.*, *97*, 1037–1053, doi:10.1130/0016-7606(1986)97<1037:DOOWAT>2.0.CO;2.

Plescia, J. B., G. J. Calderone, and L. W. Snee (1994), Paleomagnetic analysis of Miocene basalt flows in the Tehachapi Mountains, California, *U.S. Geol. Surv. Bull.*, *2100*, 11 pp.

Postlethwaite, C. E. (1983), The structural geology of the western Rand Mountains, northwestern Mojave Desert, California, M.S. thesis, Iowa State Univ., Ames.

Postlethwaite, C. E., and C. E. Jacobson (1987), Early history and reactivation of the Rand Thrust, southern California, *J. Struct. Geol.*, *9*, 195–205, doi:10.1016/0191-8141(87)90025-3.

Powell, R. E. (1993), Balanced palinspastic reconstruction of pre-late Cenozoic paleogeology, southern California: Geologic and kinematic constraints on evolution of the San Andreas fault system, in *San Andreas Fault System; Displacement, Palinspastic Reconstruction, and Geologic Evolution*, edited by R. E. Powell, R. J. Weldon II, and J. C. Matti, *Mem. Geol. Soc. Am.*, *178*, 1–106.

Ramsay, J. G. (1967), *Folding and Fracturing of Rocks*, 568 pp., McGraw-Hill, New York.

Reitz, A. (1986), The geology and petrology of the northern San Emigdio plutonic complex, San Emigdio Mountains, southern California, M.A. thesis, Univ. of Calif., Santa Barbara.

Ring, U., M. T. Brandon, S. D. Willett, and G. S. Lister (1999), Exhumation processes, in *Exhumation Processes: Normal Faulting, Ductile Flow and Erosion*, edited by U. Ring et al., *Geol. Soc. Spec. Publ.*, *154*, 1–27, doi:10.1144/GSL.SP.1999.154.01.01.

Ross, D. C. (1976), Reconnaissance geologic map of pre-Cenozoic basement rocks, northern Santa Lucia Range, Monterey County, California, *U.S. Geol. Surv. Misc. Field Stud. Map*, *MF-750*, 7 pp.

Ross, D. C. (1986), Basement-rock correlations across the White Wolf-Breckenridge-southern Kern Canyon fault zone, southern Sierra Nevada, California, *U.S. Geol. Surv. Bull.*, *1651*, 25 pp.

Ross, D. C. (1989), The metamorphic and plutonic rocks of the southernmost Sierra Nevada, California, and their tectonic framework, *U.S. Geol. Surv. Prof. Pap.*, *1381*, 159 pp.

Ross, T. M., B. P. Luyendyk, and R. B. Haston (1989), Paleomagnetic evidence for Neogene clockwise tectonic rotations in the central Mojave Desert, *Calif. Geol.*, *17*, 470–473.

Ruppert, S., M. M. Fliedner, and G. Zandt (1998), Thin crust and active upper mantle beneath the southern Sierra Nevada in the western United States, *Tectonophysics*, *286*, 237–252, doi:10.1016/S0040-1951(97)00268-0.

Saleeby, J. (2003), Segmentation of the Laramide slab; evidence from the southern Sierra Nevada region, *Geol. Soc. Am. Bull.*, *115*, 655–668, doi:10.1130/0016-7606(2003)115<0655:SOTLSF>2.0.CO;2.

Saleeby, J. B., D. B. Sams, and R. W. Kistler (1987), U/Pb zircon, strontium, and oxygen isotopic and geochronological study of the southernmost Sierra Nevada Batholith, California, *J. Geophys. Res.*, *92*, 10,443–10,466, doi:10.1029/JB092iB10p10443.

Saleeby, J., M. Ducea, and D. Clemens-Knott (2003), Production and loss of high-density batholithic root, southern Sierra Nevada, California, *Tectonics*, *22*(6), 1064, doi:10.1029/2002TC001374.

Saleeby, J., K. A. Farley, R. W. Kistler, and R. J. Fleck (2007), Thermal evolution and exhumation of deep-level batholithic exposures, southernmost Sierra Nevada, California, *Spec. Pap. Geol. Soc. Am.*, *419*, 39–66.

Saleeby, J., Z. Saleeby, E. Nadin, and G. Mahéo (2009), Step-over in the structure controlling the regional west tilt of the Sierra Nevada microplate: Eastern escarpment system to Kern Canyon system, *Int. Geol. Rev.*, *51*, 634–669, doi:10.1080/00206810902867773.

Schmid, S. M., and M. Casey (1986), Complete fabric analysis of some commonly observed quartz c-axis patterns, in *Mineral and Rock Deformation: Laboratory Studies*, *Geophys. Monogr. Ser.*, vol. 36, edited by B. E. Hobbs and H. C. Heard, pp. 263–286, AGU, Washington, D. C.

Searle, M. P., R. L. Simpson, R. D. Law, R. R. Parrish, and D. J. Waters (2003), The structural geometry, metamorphic and magmatic evolution of the Everest Massif, High Himalaya of Nepal–south Tibet, *J. Geol. Soc.*, *160*, 345–366, doi:10.1144/0016-764902-126.

Sharry, J. (1981), The geology of the western Tehachapi Mountains, California, Ph.D. thesis, Mass. Inst. of Technol., Cambridge.

Simpson, C. (1990), Microstructural evidence for northeastward movement on the Chocolate Mountains fault zone, southeastern California, *J. Geophys. Res.*, *95*, 529–537, doi:10.1029/JB095iB01p00529.

ten Grotenhuis, S. M., R. A. J. Trouw, and C. W. Passchier (2003), Evolution of mica fish in mylonitic rocks, *Tectonophysics*, *372*, 1–21, doi:10.1016/S0040-1951(03)00231-2.

Vanderhaeghe, O., C. Teyssier, and R. Wysoczanski (1999), Structural and geochronological constraints on the role of partial melting during the formation of the Shuswap metamorphic core complex at the latitude of the Thor-Odin dome, British Columbia, *Can. J. Earth Sci.*, *36*, 917–943, doi:10.1139/cjes-36-6-917.

Vargo, J. M. (1972), Structural geology of a portion of the eastern Rand Mountains, Kern and San Bernardino counties, California, M.A. thesis, Univ. of South. Calif., Los Angeles.

Wallis, S. (1992), Vorticity analysis in a metachert from the Sanbagawa Belt, SW Japan, *J. Struct. Geol.*, *14*, 271–280, doi:10.1016/0191-8141(92)90085-B.

Wallis, S. (1995), Vorticity analysis and recognition of ductile extension in the Sanbagawa Belt, SW Japan, *J. Struct. Geol.*, *17*, 1077–1093, doi:10.1016/0191-8141(95)00005-X.

Wells, M. L., and T. D. Hoisch (2008), The role of mantle delamination in widespread Late Cretaceous extension and magmatism in the Cordilleran Orogen, western United States, *Geol. Soc. Am. Bull.*, *120*, 515–530, doi:10.1130/B26006.1.

Wells, M. L., M. A. Beyene, T. L. Spell, J. L. Kula, D. M. Miller, and K. A. Zanetti (2005), The Pinto shear zone: A Laramide synconvergent extensional shear zone in the Mojave Desert region of the southwestern United States, *J. Struct. Geol.*, *27*, 1697–1720, doi:10.1016/j.jsg.2005.03.005.

Wernicke, B. (1992), Cenozoic extensional tectonics of the U.S. Cordillera, in *The Geology of North America*, vol. G-3, *The Cordilleran Orogen: Conterminous U.S.*, edited by B. C. Burchfiel et al., pp. 553–582, Geol. Soc. of Am., Boulder, Colo.

Wilson, E. L., and D. R. Prothero (1997), Magnetic stratigraphy and tectonic rotations of the middle-upper Miocene "Santa Margarita" and Chanac formations, north-central Transverse Ranges, California, in *Geology of the Western Cordillera*: *Perspectives From Undergraduate Research*, *Book*, vol. 82, edited by G. H. Girty, R. E. Hanson, and J. D. Cooper, pp. 35–48, Pac. Sect., Soc. of Econ. Paleontol. and Mineral., Fullerton, Calif.

Wood, D. J. (1997), Geology of the eastern Tehachapi Mountains and Late Cretaceous-early Cenozoic tectonics of the southern Sierra Nevada region, Kern County, California, Ph.D. thesis, Calif. Inst. of Technol., Pasadena.

Wood, D. J., and J. B. Saleeby (1997), Late Cretaceous-Paleocene extensional collapse and disaggregation of the southernmost Sierra Nevada Batholith, *Int. Geol. Rev.*, *39*, 973–1009, doi:10.1080/00206819709465314.

Xypolias, P. (2009), Some new aspects of kinematic vorticity analysis in naturally deformed quartzites, *J. Struct. Geol.*, *31*, 3–10, doi:10.1016/j.jsg.2008.09.009.

Yan, Z., R. W. Clayton, and J. Saleeby (2005), Seismic refraction evidence for steep faults cutting highly attenuated continental basement in the central Transverse Ranges, California, *Geophys. J. Int.*, *160*, 651–666, doi:10.1111/j.1365-246X.2005.02506.x.

Yin, A. (2002), Passive-roof thrust model for the emplacement of the Pelona-Orocopia schist in southern California, United States, *Geology*, *30*, 183–186, doi:10.1130/0091-7613(2002)030<0183:PRTMFT>2.0.CO;2.

A. D. Chapman, S. Kidder, and J. B. Saleeby, Division of Geological and Planetary Sciences, California Institute of Technology, 1200 E. California St., Pasadena, CA 91125, USA. (alan@gps.caltech.edu)

M. N. Ducea, Department of Geosciences, University of Arizona, 1040 East Fourth St., Tucson, AZ 85721, USA.